Dynein Separately Partners with NDE1 and Dynactin To Orchestrate T Cell Focused Secretion

Shubhankar Nath,* Laura Christian,† Sarah Youngsun Tan,† Sanghee Ki,* Lauren I. R. Ehrlich,* and Martin Poenie*

Helper and cytotoxic T cells accomplish focused secretion through the movement of vesicles toward the microtubule organizing center (MTOC) and translocation of the MTOC to the target contact site. In this study, using Jurkat cells and OT-I TCR transgenic primary murine CTLs, we show that the dynein-binding proteins nuclear distribution E homolog 1 (NDE1) and dynactin (as represented by p150^{Glued}) form mutually exclusive complexes with dynein, exhibit nonoverlapping distributions in target-stimulated cells, and mediate different transport events. When Jurkat cells expressing a dominant negative form of NDE1 (NDE1–enhanced GFP fusion) were activated by *Staphylococcus* enterotoxin E–coated Raji cells, NDE1 and dynein failed to accumulate at the immunological synapse (IS) and MTOC translocation was inhibited. Knockdown of NDE1 in Jurkat cells or primary mouse CTLs also inhibited MTOC translocation and CTL-mediated killing. In contrast to NDE1, knockdown of p150^{Glued}, which depleted the alternative dynein/dynactin complex, resulted in impaired accumulation of CTLA4 and granzyme B–containing intracellular vesicles at the IS, whereas MTOC translocation was not affected. Depletion of p150^{Glued} in CTLs also inhibited CTL-mediated lysis. We conclude that the NDE1/Lissencephaly 1 and dynactin complexes separately mediate two key components of T cell–focused secretion, namely translocation of the MTOC and lytic granules to the IS, respectively. *The Journal of Immunology*, 2016, 197: 2090–2101.

T cells typically eliminate pathogens through the cytoskeleton-directed focused secretion of effector molecules (1–3). The importance of secretion to cytotoxic and NK cell function in immunity is seen in primary hemophagocytic and Chédiak–Higashi syndromes and in inhibition of cytotoxicity in tumor microenvironments (4–8). Typically, this process takes place in a series of steps beginning with the formation of a specialized T cell/target contact known as the immunological synapse (IS) (9, 10). This is followed by translocation of the microtubule organizing center (MTOC) to the IS, which often brings secretory vesicles with it, although vesicles can also accumulate after the MTOC has translocated (11–13). Similar mechanisms appear to operate in certain T helper secretory events (14, 15).

At present, the mechanism of MTOC movement toward the synapse is not fully understood and is somewhat controversial. Alternative models of MTOC translocation posit either a dynein- or actin-dependent mechanism for driving MTOC movements. Dynein is a minus end–directed microtubule motor protein that if anchored at the IS could reel in microtubules and pull the MTOC up to the IS (16). Variants of the dynein-based models either propose that dynein causes microtubules to loop through the IS and continue to slide rearward (11, 17, 18) or that microtubules plus ends depolymerize as they move toward the IS (19), perhaps similar to the model for chromosome-to-pole movements. The actin-based model proposes that microtubules become linked to a patch of newly polymerized actin at center of the IS. As the patch of actin expands to form a peripheral ring, microtubules would be pulled laterally, driving the MTOC forward toward the IS.

Evidence that dynein is involved in MTOC translocation is derived from studies showing that dynein accumulates at the IS following T cell activation, and that small interfering RNA (siRNA)–mediated depletion of the dynein H chain blocked MTOC translocation (18). Additionally, in Jurkat cells, reduced expression of ADAP, a scaffolding protein anchored to the IS, led to a loss of dynein at the synapse and failure of MTOC translocation (17). Finally, the small molecule dynein inhibitor, ciliobrevin, was shown to block MTOC translocation (19).

Dynein is also needed to move secretory vesicles along microtubules toward the MTOC (20). Clustering of vesicles around the MTOC allows their movement en masse with the MTOC as it translocates. Alternatively, after the MTOC has translocated to the IS, vesicles can still move along microtubules from the cell periphery toward the MTOC such that they concentrate at the synapse (12, 21).

That the same dynein motor carries out such distinctly different processes raises the question of how these processes are differentially regulated and coordinated. Dynein is known to form two different complexes, one with nuclear distribution E homolog 1 (NDE1) and Lissencephaly 1 (Lis1) (22) and the other with dynactin, a multisubunit complex whose largest subunit is p150^{Glued} (23). We hypothesized that these two different dynein complexes were responsible

*Department of Molecular Biosciences, University of Texas at Austin, Austin, TX 78712; and †Department of Molecular Cell and Developmental Biology, University of Texas at Austin, Austin, TX 78712

ORCIDs: 0000-0001-5778-7615 (S.N.); 0000-0003-3141-1710 (L.C.); 0000-0002-3428-4676 (S.Y.T.); 0000-0002-1697-1755 (L.I.R.E.); 0000-0003-2524-4039 (M.P.).

Received for publication February 1, 2016. Accepted for publication July 14, 2016.

This work was supported in part by National Institutes of Health Grant R01 AI104870 (to L.I.R.E).

Address correspondence and reprint requests to Dr. Martin Poenie, University of Texas at Austin, Department of Molecular Biosciences, 2401 Speedway, PAT 543C, Austin, TX 78712. E-mail address: poenie@austin.utexas.edu

The online version of this article contains supplemental material.

Abbreviations used in this article: CTB, CellTracker Blue; DIC, dynein intermediate chain; DISC1, disrupted in schizophrenia 1; EGFP, enhanced GFP; IS, immunological synapse; Lis1, Lissencephaly 1; mEGFP, monomeric enhanced GFP; MTOC, microtubule organizing center; NDE1, nuclear distribution E homolog 1; PI, propidium iodide; SEE, *Staphylococcus* enterotoxin E; shRNA, short hairpin RNA; siRNA, small interfering RNA; TRITC, tetramethylrhodamine isothiocyanate; WT, wild-type.

for different aspects of the secretory process, one for MTOC translocation and the other for vesicle movements.

In this study, we employed the human Jurkat T cell line and OT-I TCR transgenic murine CTLs to examine the role of these two complexes in MTOC translocation, vesicle delivery to the IS, and CTL-mediated target cell lysis. We found that these proteins form mutually exclusive complexes with the dynein intermediate chain (DIC) and differ in their intracellular distributions and transport functions. Upon TCR ligation, the NDE1/Lis1/dynein complex moves to the IS where, similar to dynein and Lis1, it forms a ring-like structure corresponding to the peripheral supramolecular activation cluster of the IS (10). Depletion of NDE1 or expression of a dominant-negative enhanced GFP (EGFP)–NDE1 construct in Jurkat cells prevented dynein accumulation at the IS and blocked MTOC translocation. When NDE1 was depleted in OT-I CTLs, both MTOC translocation and target cell lysis were greatly reduced. In contrast, p150^{Glued} did not form a peripheral ring at the IS and was not required for MTOC translocation in Jurkat cells, but it was needed for clustering of vesicles around the MTOC and for their accumulation at the central supramolecular activation cluster. Furthermore, depletion of p150^{Glued} in OT-I CTLs impaired recruitment of cytotoxic granules to the IS and lysis of target cells.

Although NDE1 and p150^{Glued} formed mutually exclusive complexes with the DIC, we found that both complexes bound to disrupted in schizophrenia 1 (DISC1). DISC1 is a scaffold protein that in neurons is known to interact with dynein complexes and plays important roles in a variety of nerve cell functions, including nuclear movements, neuronal migration, delivery of synaptic vesicles to nerve terminals, cell adhesion, and cell signaling (24–31). In Jurkat cells, DISC1 concentrates at the IS upon TCR engagement and might provide a higher order of regulation for both dynein complexes.

Materials and Methods

Cell lines, reagents, and Abs

Jurkat T cell line (clone E6-1) and Raji human Burkitt's lymphoma B cell line were obtained from American Type Culture Collection (Manassas, VA). Cell culture media including RPMI 1640 (catalog no. 31800-014) and Opti-MEM (catalog no. 31985-070) were obtained from Life Technologies. Colchicine (catalog no. C9754), mitomycin C (catalog no. M4287), puromycin (catalog no. P8833), and BSA (catalog no. A7906) were obtained from Sigma-Aldrich. Heat-inactivated FBS was obtained from Atlanta Biologicals (Flowery Branch, GA, catalog no. S11550). CellTracker Blue (CTB) was purchased from Invitrogen (catalog no. C211). Purified *Staphylococcus* enterotoxin E (SEE) was obtained from Toxin Technology (Sarasota, FL, catalog no. ET404). OVA fragment (chicken, 257–264 aa, SIINKEKL-OH) peptide was purchased from New England Peptide (Gardner, MA, catalog no. BP10-915).

Jurkat and Raji cells were grown in RPMI 1640 medium supplemented with 10% FBS (v/v), 50 μM 2-ME, 24 mM $NaHCO_3$, 1 mM pyruvate, 1 mM glutamine, 100 U/ml penicillin, and 100 μg/ml streptomycin. Cells were cultured at 37˚C in a 5% CO_2 atmosphere.

Abs used in this project are rabbit anti-NDE1 Ab (catalog no. 10233-1-AP; Proteintech Group), rat anti-NDEL1 Ab (a gift from Dr. Atsushi Kamiya, John Hopkins University), mouse anti-DIC IgG Ab clone 74.1 (catalog no. MMS-400P; Covance), mouse anti-DIC IgM Ab clone 70.1 (catalog no. D5167; Sigma-Aldrich), mouse anti-Lis1 Ab (catalog no. L7391; Sigma-Aldrich), mouse anti–β-tubulin Ab (catalog no. T4026; Sigma-Aldrich), mouse anti-p150^{Glued} Ab (catalog no. 610474; BD Transduction Laboratories), mouse anti-human Vβ8 Ab (catalog no. 555604; BD Pharmingen), rabbit anti-DISC1 Ab (catalog no. PA2023; Boster Biological Technology and catalog no. S0371; Epitomics), rabbit anti-granzyme B Ab (catalog no. A-2557; ABclonal), rabbit anti-GFP Ab (catalog no. A11122; Thermo Fisher Scientific), unconjugated rabbit anti-mouse IgG secondary Ab (catalog no. 31190; Thermo Fisher Scientific), tetramethylrhodamine isothiocyanate (TRITC)–conjugated goat anti-mouse IgG-Fc–specific Ab (catalog no. T7657; Sigma-Aldrich), FITC-conjugated goat anti-mouse IgG Ab (catalog no. F2012; Sigma-Aldrich), Alexa Fluor 594–conjugated goat anti-rabbit Ab (catalog no. A-11037; Thermo Fisher Scientific), TRITC-conjugated phalloidin (catalog no. P1951; Sigma-Aldrich), HRP-conjugated goat anti-mouse IgG Ab (catalog no. 31430; Thermo Fisher Scientific), and HRP-conjugated goat anti-rabbit IgG Ab (catalog no. sc-2004; Santa Cruz Biotechnology).

Cloning of NDE1 constructs

Total mRNA was isolated from Jurkat cells using a GenElute mammalian total RNA miniprep kit (catalog no. RTN10; Sigma-Aldrich) and a cDNA library was created by RT-PCR using a Moloney murine leukemia virus reverse transciptase first-strand cDNA synthesis kit (catalog no. MM070110; Epicentre, Madison, WI) and stored at −80˚C until use.

To create the EGFP-NDE1 construct, NDE1 transcript variant 1 (accession no. NM_001143979) was amplified from a Jurkat cDNA library using the following primers: NDE1 forward, 5′-ATGGAGGACTCCGGAAAGACT-3′, reverse, 5′-TCAGCAGGAGCTGGACGA-3′. The coding region (CDS) was cloned into pEGFP-C1 plasmid between Kpn1 and Xma1 restriction sites. This led to N-terminal EGFP fused to NDE1 sequence.

To create the NDE1-EGFP construct, the coding sequence from EGFP-NDE1 plasmid was subcloned into pEGFP-N1 plasmid between XhoI and HindIII restriction sites. The plasmid was further modified to disrupt the Kozak consensus sequence at the beginning of EGFP to abolish EGFP only expression from the plasmid. Additionally, a Kozak sequence was added at the beginning of the start codon of NDE1 to enhance its expression in mammalian cells.

To create the NDE1–monomeric EGFP (mEGFP) or mEGFP-NDE1 constructs (monomeric EGFP), a point mutation was created at A206K position of EGFP of the preceding plasmid following Stratagene site-directed point mutagenesis protocol using the following primers: mEGFPa206k forward, 5′-CTGAGCACCCAGTCCAAACTGAGCAAAGACCCC-3′, reverse, 5′-GGGGTCTTTGCTCAGTTTGGACTGGGTGCTCAG-3′. The presence of the NDE1 coding region in each plasmid was confirmed by sequencing.

Cloning of CTLA4 plasmid

The mouse CTLA4–yellow fluorescent protein construct was a gift from Dr. James Allison (MD Anderson Cancer Center, Houston, TX). To obtain CTLA4–mCherry, the CTLA4 coding sequence was subcloned into pIRES-PURO3-mCherry vector between ClaI and NheI restriction enzyme sites. pIRES-PURO3-mCherry plasmid was provided by Dr. Roger Tsien (University of California San Diego, San Diego, CA) and was subsequently modified to insert several restriction enzyme sites following standard PCR protocol. mCherry was placed on the 3′ end of CTLA4 to avoid possible complications with membrane insertion.

Transfection of plasmids and siRNAs in Jurkat cells

For each transfection of plasmids, 15×10^6 wild-type (WT) Jurkat cells were washed in sterile PBS (3.8 mM KCl, 1.2 mM KH_2PO_4, 139 mM NaCl, 3.15 mM Na_2HPO_4, 1 mM $MgSO_4$ [pH 7.2]), resuspended in 400 μl of serum-free Opti-MEM medium, and transferred into a 0.4-cm Gene Pulser cuvette (catalog no. 165-2081; Bio-Rad). The cells were incubated at room temperature for 5 min with 15 μg of appropriate plasmid maxiprep before electroporation using a Bio-Rad Gene Pulser II machine with 950 μF and 250 V. The cells were then resuspended in complete growth medium and incubated with 5% CO_2 at 37˚C. Selection with G418 or puromycin antibiotic started 24 h after transfection and continued for 2 wk before sorting using a FACSAria cell sorter (BD Biosciences).

For protein knockdown in Jurkat cells, a pool of siRNA oligonucleotides targeting NDE1 transcripts (catalog no. SASI_Hs01_00074363-66; Sigma-Aldrich), p150^{Glued} (catalog no. SASI_Hs01_00065675-78; Sigma-Aldrich), or siRNA universal negative control (catalog no. SIC002; Sigma-Aldrich) were introduced into cells by electroporation as described above. To determine the amount of protein expression, 1×10^6 cells were collected at 0, 24, 48, and 72 h posttransfection. Cells were then lysed in RIPA buffer, boiled with 2× SDS lysis buffer at 95˚C for 5 min, and expression was analyzed on Western blots. For both NDE1 and p150^{Glued}, the lowest expression was seen at the 48 h time point and these cells were used for subsequent experiments.

Preparation of cell conjugates and immunostaining

Coverslips were cleaned in ethanol in the presence of 10% concentrated potassium hydroxide. They were then coated with 1 mg/ml poly-L-lysine, rinsed in distilled water, air dried, and used immediately or stored at 4˚C for future use. Raji cells were washed and incubated with SEE for 1 h in serum-free RPMI 1640 medium. For identification, Raji cells were labeled with CellTracker Blue (CTB) for the last 15 min. Raji cells were then paired with Jurkat cells by copelleting the cells at 1000 × *g* for 5 min.

Pellets were then gently resuspended and cells were adhered to polylysine-coated coverslips at 37°C for 10 min. Cells on coverslips were fixed in PBS containing 1 mM $CaCl_2$, 5 mM glucose, and 4% freshly prepared depolymerized paraformaldehyde for 30 min at room temperature followed by permeabilizing for 15 min in a prechilled 1:1 acetone/methanol solution on ice. Fixed cells were then blocked with 5% goat serum and 0.5% Tween 20 at room temperature for 30 min. Primary and secondary Ab incubation was done sequentially for 1 h each at room temperature in blocking solution. The Ab concentrations used were as recommended by the manufacturers. The coverslips were mounted on glass slides using ProLong diamond antifade reagent and sealed with nail polish.

For microtubule depolymerization assays, Jurkat cells were incubated with either DMSO (vehicle) or 10 μM colchicine for 15 min before being paired with SEE-coated Raji cells.

Immunoprecipitation and Western blots

To prepare cell lysates for immunoprecipitation, 10^7 cells per sample were pelleted, washed in PBS, and mixed with ice-cold RIPA buffer (100 mM Tris [pH 8], 50 mM NaCl, 0.25% Triton X-100, 1 mM EDTA, 10 mM NaF, 2 mM Na_3VO_4, 2× Roche mini EDTA-free protease inhibitor). The lysate was homogenized by pipetting through a 21-gauge sterile needle. Cellular debris were separated by centrifugation at 10,000 rpm for 10 min. The supernatant was precleared with protein A–agarose beads for 1 h and then transferred to a tube containing protein A –agarose beads coupled to Ab and incubated for 3 h at 4°C. The beads were subsequently pelleted at 1000 × *g* for 3 min, washed three times with ice-cold RIPA lysis buffer, and boiled at 95°C for 5 min with 2× SDS-protein loading buffer. Unless otherwise mentioned, 10% of the supernatant of the immunoprecipitation reaction was processed in the same way as the samples and used as input on SDS-PAGE analysis.

Precleared whole-cell lysate or immunoprecipitation samples were run on 10% polyacrylamide gels (SDS-PAGE). Proteins from SDS-PAGE were wet transferred to 0.2-μm nitrocellulose membrane at 100 V for 1 h. The membrane was blocked in 5% nonfat milk in TBS and incubated with primary Ab solution (5% BSA with 0.05% Tween 20 in TBS, 25 mM Tris, 137 mM NaCl, 2.7 mM KCl) overnight at 4°C shaker followed by washing and 1 h incubation with corresponding HRP-conjugated secondary Ab solution (5% nonfat milk in TBS) on a 50-rpm shaker at room temperature.

Calcium measurements

Cells were washed and resuspended in PBS containing 5 mM glucose, 1 mM $CaCl_2$, and 1% FBS to a final concentration of 10^6 cells/ml and incubated at 37°C for 30 min in presence 1 μM indo-1-AM (catalog no. I1203; Thermo Fisher Scientific) or with DMSO vehicle. Cells were washed, resuspended in the PBS buffer, incubated for an additional 10 min, and then transferred to a standard fluorometer cuvette. Measurements were performed in a fluorometer equipped with dual emission detectors, a water-jacketed cuvette holder maintained at 37°C, and a magnetic stirrer to keep the cells in suspension (Photon Technology International, Birmingham, NJ). Fluorescence was excited at 354 nm and the emission collected at 404 and 485 nm. After baseline measurements were obtained, 500 ng/ml anti-Vβ8 Ab was then added followed by 500 ng/ml unconjugated rabbit anti-mouse IgG secondary Ab. At the end of each trace, ionomycin was added to 2 μM followed by 0.1 mg/ml digitonin and then 2 mM EGTA together with 6 mM Tris base.

Cloning of lentiviral short hairpin RNA constructs

The target sequences for knockdown of mouse NDE1 were as follows: 5′-CTTCACTGGCTACTAACTTAT-3′ (N1), 5′-AGTACCAGTGTGGGCGATAAA-3′ (N2), and 5′-ACCAACTGCAGAAATACATTA-3′ (N3). The nontarget base scrambled negative control sequence was 5′-CCTAAGGTTAAGTCGCCCTCG-3′ (C1). The target sequences for knockdown of mouse $p150^{Glued}$ were as follows: 5′-AGTGCAGTGTGGACGTGTATA-3′ (P1), 5′-CCATGCAAGAAGGCGAGTATG-3′ (P2), and 5′-CAGACGAGCGAATCGAGAAAG -3′ (P3). Primers were purchased from Sigma-Aldrich and cloned into pLKO.1-TRC cloning vector (catalog no. 10878; Addgene) as described by Moffat et al. (32). Insertion of intended sequences into the plasmid was confirmed by DNA sequencing. Plasmid constructs were transfected into HEK293 cells using Xfect transfection reagent (catalog no. 631317; Clontech). Viral supernatant was collected 48 h posttransfection, filtered using a 0.45-μm syringe filter, mixed with 4 μg/ml Polybrene (catalog no. H9268; Sigma-Aldrich), and then stored at −80°C until used.

Lentiviral knockdown of NDE1 and $p150^{Glued}$ in OT-I primary cells

Naive T cells were isolated from spleens of OT-I transgenic mice and were stimulated with syngeneic splenocytes pulsed with 1 μM SIINFEKL. Splenocytes were pretreated with 50 μg/ml mitomycin C for 2 h and thoroughly washed before peptide loading. CTLs were maintained in the same complete growth medium that was used for Jurkat cells but supplemented with 20 U/ml IL-2. After 2 d of stimulation, 0.5×10^6 CTLs were collected, washed, and transduced with corresponding lentiviral supernatants (multiplicity of infection of ∼5–10) for 10 h. Spinfection was performed at 2400 rpm for 30 min at 30°C. Cells were resuspended in fresh medium after 10 h. Selection of transduced CTLs was started 48 h after transduction using puromycin (1 μg/ml initially for 1 d and at 2 μg/ml for an additional 3 d before analysis of expression on Western blots).

For immunostaining, EL4 target cells were pulsed with 1 μM SIINFEKL peptide for 1 h and labeled with CTB for 15 min. Cells were washed thoroughly before CTL-EL4 conjugates were prepared. Other conditions for immunofluorescence, Western blot, or immunoprecipitation experiments using primary cells remained the same as described above.

Mouse CTL-mediated cytotoxicity assay

A flow cytometry–based cytotoxicity assay was adapted from previously described protocols (33, 34). Briefly, NDE1-specific short hairpin RNA (shRNA) (N2)– and $p150^{Glued}$-specific shRNA (P1)–treated CTLs, which showed highest level of corresponding protein knockdown, and scrambled control shRNA (C1)–treated CTLs were mixed with EL4 target cells in a round-bottom 96-well plate. To distinguish the target cells from the CTLs, EL4 cells were labeled with 250 nM CFSE for 30 min in PBS and then washed twice. Labeled EL4 cells were then used directly for cytotoxicity assay or pulsed with 1 μM SIINFEKL peptide for 1 h. EL4 cells (10^4) per well were mixed with corresponding CTLs at a ratio of 1:1, 4:1, and 10:1 (E:T) to a final volume of 150 μl in each well. The plate was incubated at 37°C for 6 h. Propidium iodide (PI) was added to a concentration of 100 μg/ml at the end of the assay and the cells were immediately analyzed for PI^+ and $CFSE^+$ cells using a BD Accuri C6 Plus flow cytometer. FACS data were analyzed using FlowJo software and presented after background normalization.

PCR analysis of NDE1 isoforms in mouse CTLs

The total mRNA pool was isolated from mouse CTLs and cDNA was synthesized following the protocol mentioned above. The National Center for Biotechnology Information BLAST program was used to design primers to detect unique regions of four commonly reported mouse NDE1 isoforms. The primers used were as follows: isoform a (NM_023317.2), forward, 5′-AAGAGCCAAACGAGCCACA-3′, reverse, 5′-AAGCGTTTTCCTGACCCTTTATC-3′; isoform b (NM_001114085.1), forward, 5′-GAACCGGGACCTCTTGTCAG-3′, reverse, 5′-GGAAGGGATCCTTTATCGCCC-3′; isoform c (NM_001285503.1), forward, 5′-GAATAACCGCCTTCGCATGG-3′, reverse, 5′-GATGAGACAGCAGTACCCCAG-3′; isoform d (NM_001285504.1), forward, 5′-AGTCTGTGAAGAGCCACAATCA-3′, reverse, 5′-CATCTCCGGCTTTACCACCC-3′.

Assessment of CTLA4- or granzyme B–containing vesicle accumulation at the IS

To quantify CTLA4-mCherry clustering at the IS, we distinguished four main vesicle patterns in Jurkat cells CLTA4-mCherry. When vesicles were observed in a band at the Jurkat/Raji interface, or in a tight cluster elsewhere in the cell, we counted the vesicles as "clustered." A second category was "unclustered," defined as cells having a large number of vesicles (at least 15) dispersed away a group of vesicles still clustered around the MTOC, to cells showing no clustering at all. A similar approach was also applied to quantify granzyme B–containing vesicles in CTLs.

Image acquisition, analysis, and data processing

The scoring of MTOC polarization has been described previously (35, 36). Briefly, a T cell was divided into four sections of equal width and assigned as region 1, 2, 3, or 4 (region 1 being the nearest to the IS). When the MTOC was located in region 1, the cell was counted as polarized.

Images were acquired using a Nikon Eclipse microscope coupled to an Andor Zyla scientific CMOS camera. Images were recorded using Micro-Manager and processed using ImageJ processing software. For determining protein accumulation at the synapse, a line (width, 70 pixels; length, 230 pixels) was drawn through conjugate pairs with the middle (pixel 115) corresponding to the IS. Background intensity obtained from a region outside the cell was subtracted and fluorescence was normalized by dividing all pixel values by the average intensity of row 1 (the rear of the Jurkat cell). Beginning with row 115, intensity values of five rows of pixels were grouped together to give one increment and used for statistics (mean ± SE of the mean). The computed mean together with error bars for each increment

was plotted against normalized intensity. A Student *t* test was performed for the first 10 increments.

Results

NDE1 is recruited to the immunological synapse

NDE1 was detected in Jurkat cells by quantitative real-time PCR (data not shown) and on Western blots as a single band at 40 kDa (Supplemental Fig. 1A). To examine the distribution of NDE1 before and after stimulation, Jurkat cells, alone or paired with SEE-coated Raji cells, were immunostained for NDE1 and tubulin. Prior to stimulation, NDE1 was observed in punctate foci distributed throughout the cytoplasm (Fig. 1A). After Jurkat cells were activated with SEE-coated Raji cells, NDE1 became concentrated at the IS (Fig. 1B).

To determine whether signal transduction through the TCR was required for NDE1 translocation, Jurkat cells were pretreated with either DMSO (vehicle) or the Src kinase inhibitor PP2, paired with SEE-coated Raji cells, and then immunostained for NDE1. NDE1 accumulated at the IS in vehicle-treated cells (Fig. 1C), whereas treatment with PP2 prevented this accumulation (Fig. 1D). Quantification of the average cellular fluorescence through the T cell–target contact site for a population of Jurkat/Raji pairs confirmed that inhibition of Src family kinases blocked translocation of NDE1 to the IS (Fig. 1E).

To determine whether dynein forms a complex with NDE1, the DIC was immunoprecipitated from Jurkat cell lysates and analyzed for dynein-binding proteins on Western blots. We observed that NDE1, Lis1, and $p150^{Glued}$ each coimmunoprecipitated with the DIC (Fig. 1F). However, when the reciprocal immunoprecipitation of NDE1 was carried out using a polyclonal anti-NDE1 Ab, the DIC and $p150^{Glued}$ were not detected in the immunoprecipitate (Fig. 1G). Failure of anti-NDE1 Ab to pull down the DIC suggested that the Ab might interfere with binding of NDE1 to dynein, an issue raised in a previous study (37). In a similar series of experiments, we also immunoprecipitated DISC1 and probed for the DIC and dynein-binding proteins. The results showed that the DIC, NDE1, Lis1, and $p150^{Glued}$ all coimmunoprecipitated with DISC1 (Supplemental Fig. 1B). Furthermore, in Jurkat cells paired with SEE-coated Raji cells, DISC1 was seen localized at the IS (Supplemental Fig. 1C–E).

Functional NDE1 is required for accumulation of dynein and Lis1 at the IS

Because anti-NDE1 Ab immunoprecipitates did not contain dynein, perhaps due to Ab and dynein binding to the same site on NDE1, we sought to determine whether immunoprecipitation of NDE1-EGFP chimeras with anti-GFP would pull down the DIC. For these studies, a series of NDE1 EGFP chimeras were constructed and tested for their ability to bind dynein, localize at the IS, and support MTOC translocation. The three most notable constructs were an N-terminal EGFP fusion to NDE1 (EGFP-NDE1) that potently blocked MTOC translocation, a C-terminal EGFP fusion to NDE1 (NDE1-EGFP) that slightly inhibited MTOC translocation, and a C-terminal mEGFP fusion to NDE1 (NDE1-mEGFP) that showed no inhibition of MTOC translocation (Fig. 2A–D). When these cells were activated by SEE-coated Raji B cells, EGFP-NDE1 remained in the cytosol, whereas both NDE1-EGFP and NDE1-mEGFP were localized at the IS (Fig. 2A–C). Other constructs had intermediate effects and were not further explored (data not shown).

Although the NDE1-EGFP construct localized at the IS and did not block MTOC translocation (Fig. 2B, 2D), neither it nor the EGFP-NDE1 construct pulled down the DIC in immunoprecipitation studies (Fig. 2E, 2F). One possible explanation was that EGFP

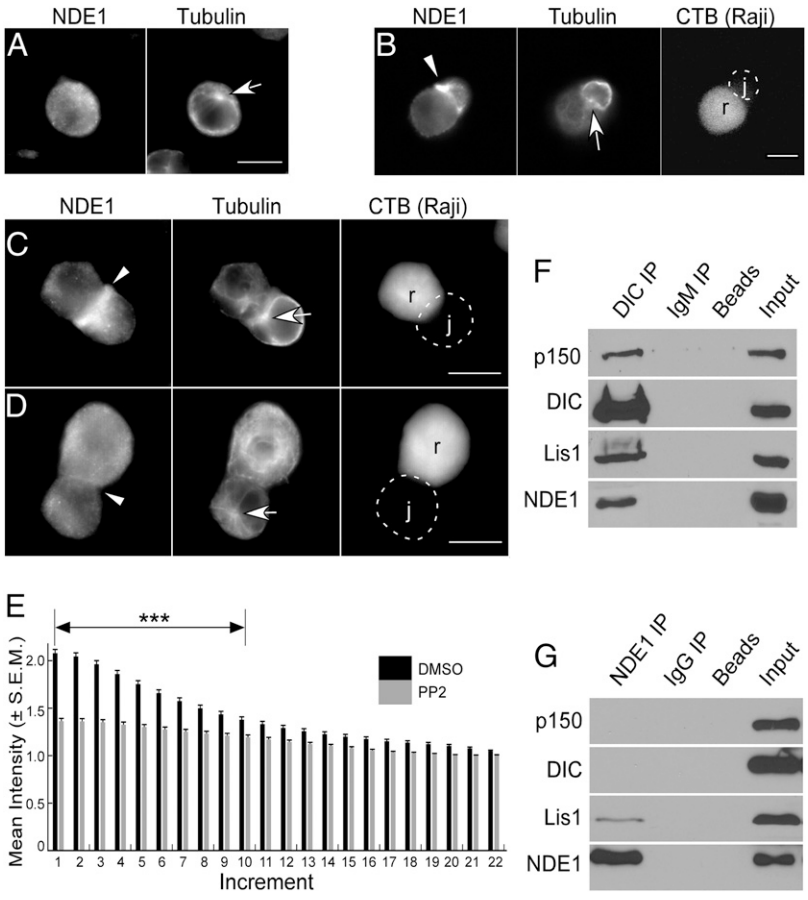

FIGURE 1. NDE1 in Jurkat cells. (**A**) Jurkat cells were fixed and immunostained for NDE1 and β-tubulin. (**B**) Jurkat cells were paired with SEE-coated Raji cells, fixed, and immunostained for NDE1 and β-tubulin. (**C**) Jurkat cells were pretreated with either DMSO vehicle or (**D**) the Src-kinase inhibitor PP2 and then paired with SEE-coated Raji B cells and immunostained for NDE1 and β-tubulin. (**E**) The distribution of NDE1 was analyzed from 46 immunostained images as described in the *Materials and Methods*. Mean intensity values ± SEM were plotted for five pixel-wide segments starting at the IS and moving to the back of the cell. (**F**) DIC was immunoprecipitated from Jurkat cell lysates using mouse anti-DIC Ab (clone 70.1). Blots were then probed for Lis1, NDE1, and $p150^{Glued}$. (**G**) NDE1 was immunoprecipitated from WT Jurkat cell lysates using polyclonal rabbit anti-NDE1 Ab and then blots were probed for Lis1, the DIC, and $p150^{Glued}$. For all imaging data, Raji cells were labeled with CTB. White arrowheads indicate the immunological synapse; white arrows indicate MTOC. Scale bars, 10 μm. $***p < 0.001$. j, Jurkat cell; r, Raji cell.

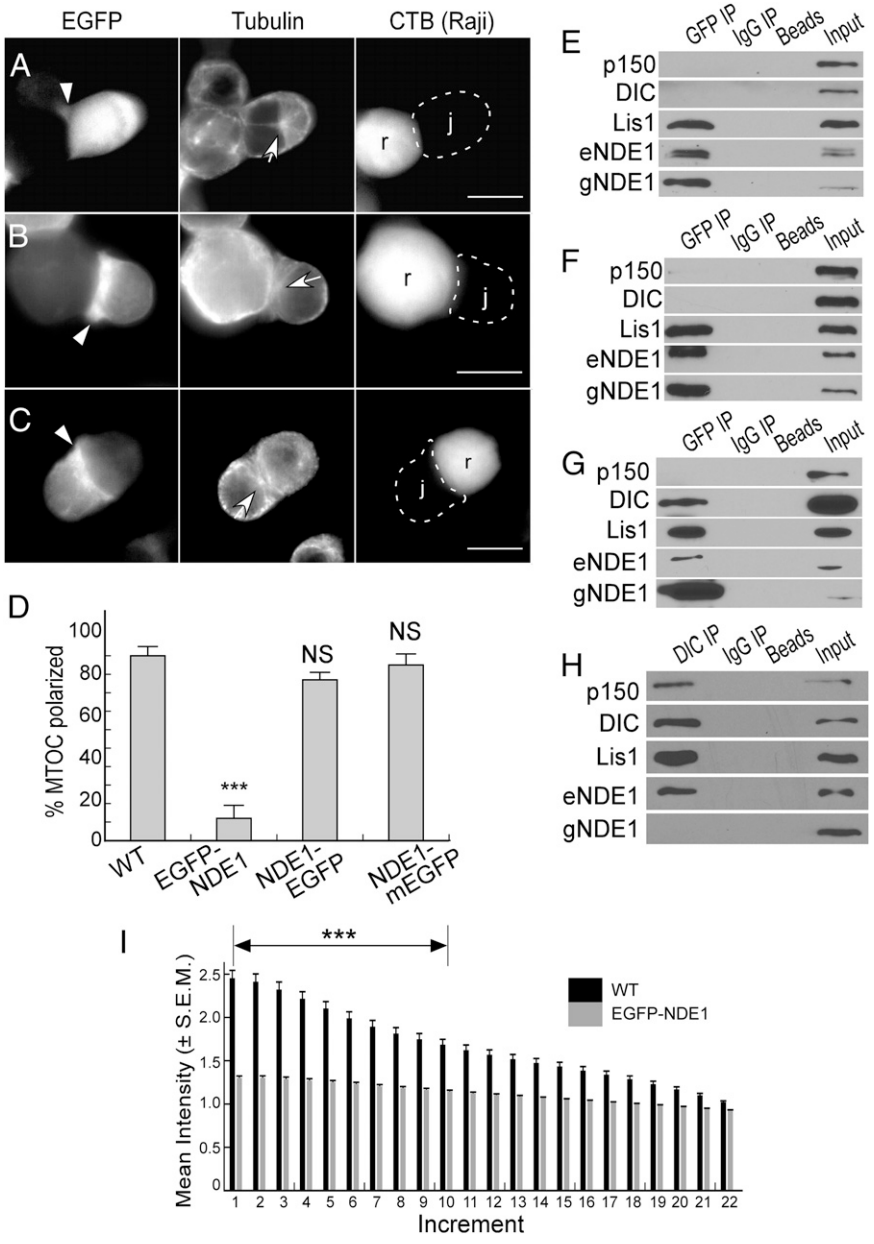

FIGURE 2. EGFP-tagged NDE1 chimeras. Jurkat cells expressing either EGFP-NDE1 (**A**), NDE1-EGFP (**B**), or NDE1-mEGFP (C-terminal, monomeric EGFP) (**C**) were paired with SEE-coated Raji cells and immunostained for β-tubulin. (**D**) MTOC polarization was analyzed from immunostained images and plotted after background subtraction (typically 20–30%). For cells expressing EGFP-NDE1, MTOC polarization was significantly inhibited ($p < 0.001$) whereas in cells expressing NDE1-EGFP or NDE1-mEGFP the effect, if any, was slight. EGFP-NDE1 (**E**), NDE1-EGFP (**F**), or NDE1-mEGFP (**G**) was immunoprecipitated from corresponding Jurkat cell lysates using an anti-GFP Ab and blots were then probed for NDE1, Lis1, $p150^{Glued}$, and the DIC. Two major NDE1 bands were identified where eNDE1 (40 kDa) corresponds to the molecular mass of endogenous NDE1, whereas gNDE1 (67 kDa) corresponds to the molecular mass of NDE1 fused to the GFP tag. This was confirmed by probing with anti-GFP. (**H**) The DIC was immunoprecipitated from NDE1-EGFP–expressing Jurkat cell lysates and probed for NDE1, NDE1-EGFP, Lis1, $p150^{Glued}$, and the DIC. For imaging studies, Raji cells were labeled with CTB. White arrowheads indicate contact sites; white arrows indicate the MTOC. Scale bars, 10 μm. (**I**) Mean DIC fluorescence intensity ± SEM was plotted for five pixel-wide segments as described previously. Data were obtained from 81 WT or EGFP-NDE1–expressing Jurkat/Raji cell pairs. ***$p < 0.001$. j, Jurkat cell; r, Raji cell.

somehow interfered with NDE1 folding and reduced its interaction with the DIC. NDE1 is thought to fold into a hairpin that brings the dynein binding sites at the N and C terminus in close proximity so as to function as one contiguous binding site. Furthermore, it is thought that NDE1 can form dimers and tetramers (22). Given that EGFP can dimerize on its own, perhaps this interfered with the normal folding or dimerization of NDE1. To address this possibility, EGFP was mutated (A206K) to give mEGFP (mEGFP-NDE1; NDE1-mEGFP) (38). When these constructs were immunoprecipitated with anti-GFP Ab and analyzed for the DIC, we found that the NDE1-mEGFP construct coimmunoprecipitated with the DIC, endogenous NDE1, and Lis1 (Fig. 2G). The mEGFP-NDE1 construct pulled down Lis1 and endogenous NDE1 but not the DIC (data not shown). When these constructs were analyzed for their impact on MTOC translocation, the data show that NDE1-mEGFP gave the same levels of MTOC translocation as did WT Jurkat cells (Fig. 2D), whereas the mEGFP-NDE1 was still inhibitory (not shown). For subsequent studies, we continued to use the original EGFP-NDE1 as a potent inhibitory construct. The observation that NDE1-mEGFP localized at the IS, did not affect MTOC polarization, and that it pulled down the DIC as well as endogenous NDE1 suggested that it was functioning normally.

Because immunoprecipitation of NDE1-EGFP using anti-GFP Ab did not pull down the DIC, we next sought to determine whether immunoprecipitation of dynein would pull down NDE1-EGFP. To test this hypothesis, we immunoprecipitated the DIC from NDE1-EGFP–expressing Jurkat cell lysates. Interestingly, we also did not detect any NDE1-EGFP in the DIC immunoprecipitates (Fig. 2H), although endogenous NDE1 was detected (Fig. 1F). These results indicate that NDE1-EGFP accumulates at the IS without binding to dynein.

Immunostaining for the DIC and Lis1 showed that both of these proteins colocalized with NDE1 at the IS in WT Jurkat/Raji pairs or in Jurkat cells expressing NDE1-EGFP or NDE1-mEGFP (Supplemental Fig. 2A–F). Alternatively, neither the DIC nor Lis1 localized at the IS in Jurkat cells expressing the dominant-negative EGFP-NDE1 (Supplemental Fig. 2G, 2H). Analysis of 81 Jurkat/Raji pairs from immunostained images showed that DIC was largely absent from the IS in Jurkat cells expressing EGFP-NDE1 proteins as compared with WT Jurkat cells (Fig. 2I).

NDE1 constructs do not block calcium signaling

In previous studies, some perturbations of dynein seemed to affect cell signaling. For example, Martín-Cófreces et al. (18) noted differences in phosphorylation in T cells overexpressing dynamitin. In other experiments, Yi et al. (19) used 50 μM ciliobrevin D to inhibit dynein. However, we found that 1 μM ciliobrevin D severely reduced calcium signaling and at 50 μM, calcium signaling was essentially abolished (Supplemental Fig. 2I). As a precaution, we thought it necessary to determine whether the expressed NDE1 constructs affected calcium signaling through the TCR. To monitor calcium signaling, these cell lines were loaded with indo-1-AM and stimulated with anti-TCR Ab. The fluorescence ratio of calcium-bound/unbound indo-1 signal obtained after subtracting the fluorescence background suggested no abnormality in calcium signaling in any of the tested cell lines (Supplemental Fig. 2J).

Depletion of NDE1 blocks MTOC translocation

Although inhibition of MTOC translocation by the dominant-negative EGFP-NDE1 construct suggested that NDE1 might be important for MTOC translocation, there is always the possibility that EGFP fusion proteins could have nonspecific effects. To further examine the role of NDE1 in MTOC translocation, NDE1 was depleted using NDE1-specific siRNA. By monitoring NDE1 expression at 24-h intervals, we found that NDE1 expression was greatly reduced 24–72 h after siRNA transfection, whereas the control siRNA had no effect (Fig. 3A). Using the 48-h time point for subsequent assays, control and knockdown cells were paired with SEE-coated Raji cells and immunostained for tubulin and NDE1. The data show that MTOC translocation was greatly reduced in the NDE1 siRNA-treated cells (Fig. 3B–D). As expected, visible NDE1 accumulation at the synapse in NDE1 knockdown cells was also greatly reduced compared with the control cells (Fig. 3E).

NDE1 depletion leads to a loss of dynein from the synapse

To determine whether NDE1 depletion prevented the recruitment of dynein to the synapse, NDE1 siRNA– and control siRNA–treated cells were paired with SEE-coated Raji cells and immunostained for the DIC. The data show that for the control siRNA–treated cells, NDE1 and DIC colocalized at the synapse as seen for untreated Jurkat cells (Fig. 3F). In cells treated with the NDE1-specific siRNA, little DIC was seen at the synapse (Fig. 3G). To quantify the difference in dynein accumulation, average pixel values were plotted as described previously. The results confirm that when NDE1 expression is reduced, little dynein accumulates at the synapse (Fig. 3H).

To determine whether reduced expression of NDE1 impacted calcium signaling or the accumulation of actin at the IS, both were also monitored in control and NDE1-depleted cells. Depletion of NDE1 had little impact on the accumulation of actin at the synapse (Fig. 3I, 3J) or on calcium signaling in response to TCR stimulation (Fig. 3K).

Accumulation of NDE1 at the synapse requires intact microtubules

The previous data showed that NDE1 translocated from the cytoplasm to the synapse when Jurkat cells were stimulated by SEE-coated Raji cells. To determine whether this translocation was microtubule-dependent, the distribution of NDE1 was monitored in colchicine-treated Jurkat/Raji pairs. NDE1 accumulation at the synapse was profoundly reduced in colchicine-treated cells compared with DMSO-treated cells (Fig. 4A, 4B). Quantitative analysis of NDE1 pixel values confirmed that intact microtubules were required for NDE1 accumulation at the IS in Jurkat cells (Fig. 4C).

NDE1 in primary mouse CTLs recapitulates the pattern seen in Jurkat cells

We next sought to determine the function of NDE1 in mouse primary CTLs. For these experiments, CTL blasts were prepared from splenocytes of OT-I mice by mixing them with mitomycin-treated C57BL/6 splenocytes in the presence of SIINFEKL peptide. Subsequently, OT-I CTLs were mixed with EL4 cells in the presence or absence of peptide and immunostained for NDE1. The results showed that in the absence of peptide NDE1 was scattered throughout the cytoplasm (Supplemental Fig. 3A, 3B). In the presence of peptide, NDE1 accumulated at the IS, similar to the results obtained using Jurkat cells (Supplemental Fig. 3C).

The dynein complexes in mouse CTLs were examined by immunoprecipitating the DIC. The results showed that NDE1, Lis1, and $p150^{Glued}$ coimmunoprecipitated with the DIC from CTL cell lysates (data not shown). Similar to the results obtained from Jurkat cells, immunoprecipitation of NDE1 did not pull down the DIC or $p150^{Glued}$ (Supplemental Fig. 3D). The only obvious difference between the results obtained using Jurkat cells or mouse CTLs was that for the CTLs, NDE1 Ig appeared to detect multiple bands on the blot, perhaps due to the presence of multiple NDE1 isoforms. To test this idea, we designed specific primers targeting four common mouse NDE1 mRNA transcripts according to the National Center for Biotechnology Information database. PCR results indicated that NDE1 isoforms b, c, and d are present in OT-I mouse CTLs whose molecular masses corresponded to the three bands seen on the blot (Supplemental Fig. 3E). Immunostaining of mouse CTL-EL4 conjugates showed that NDE1 localization at the IS overlapped that of DIC and Lis1 (Supplemental Fig. 3F, 3G).

Failure of MTOC translocation in NDE1-depleted primary mouse CTLs

To deplete NDE1 in mouse CTLs, three NDE-1 specific (N1, N2, and N3) and one base-scrambled control shRNA sequence were packaged into lentiviral particles and incubated with CTLs for 10 h. Subsequently, CTLs were selected with puromycin for 4 d. Of the three NDE1 shRNA targets, only N2 gave a strong reduction in NDE1 expression and was used for subsequent experiments (Fig. 5A).

OT-I CTLs pretreated with lentiviral NDE1-specific (N2) or scrambled control shRNA were prepared as described above and then incubated with peptide-pulsed EL4 cells. Subsequently, cells were immunostained for tubulin (Fig. 5B, 5C) and scored for MTOC translocation (Fig. 5D). For the bulk population MTOC translocation was reduced from 80 to 48% for the NDE1-specific shRNA but was not affected by the scrambled control (Fig. 5B–D, "all pairs"). However, both the Western blot and immunostaining showed a partial knockdown of NDE1 such that NDE1 could sometimes still be detected at the IS (Supplemental Fig. 3H). When NDE1 was detected at the IS, the MTOC often translocated as well. When we examined CTL conjugates that showed no obvious NDE1 at the IS, the percentage of cells showing MTOC translocation was reduced to 20% (Fig. 5D, "selected pairs").

Depletion of NDE1 reduces CTL-mediated cytotoxicity

Finally, we investigated how depletion of NDE1 affected the ability of mouse CTLs to lyse antigenic targets. CTLs transduced with either NDE1 or control shRNAs (as described above) were incubated for 6 h with untreated EL4 or peptide-pulsed EL4 target cells at various E:T ratios (1:1, 4:1, or 10:1). Subsequently, PI was added to label the dead cells. Flow cytometry was used to quantify CFSE-labeled target cells and PI-labeled dead cells as described in *Materials and Methods*. Depletion of NDE1 significantly inhibited CTL-mediated target cell lysis, compared with control groups

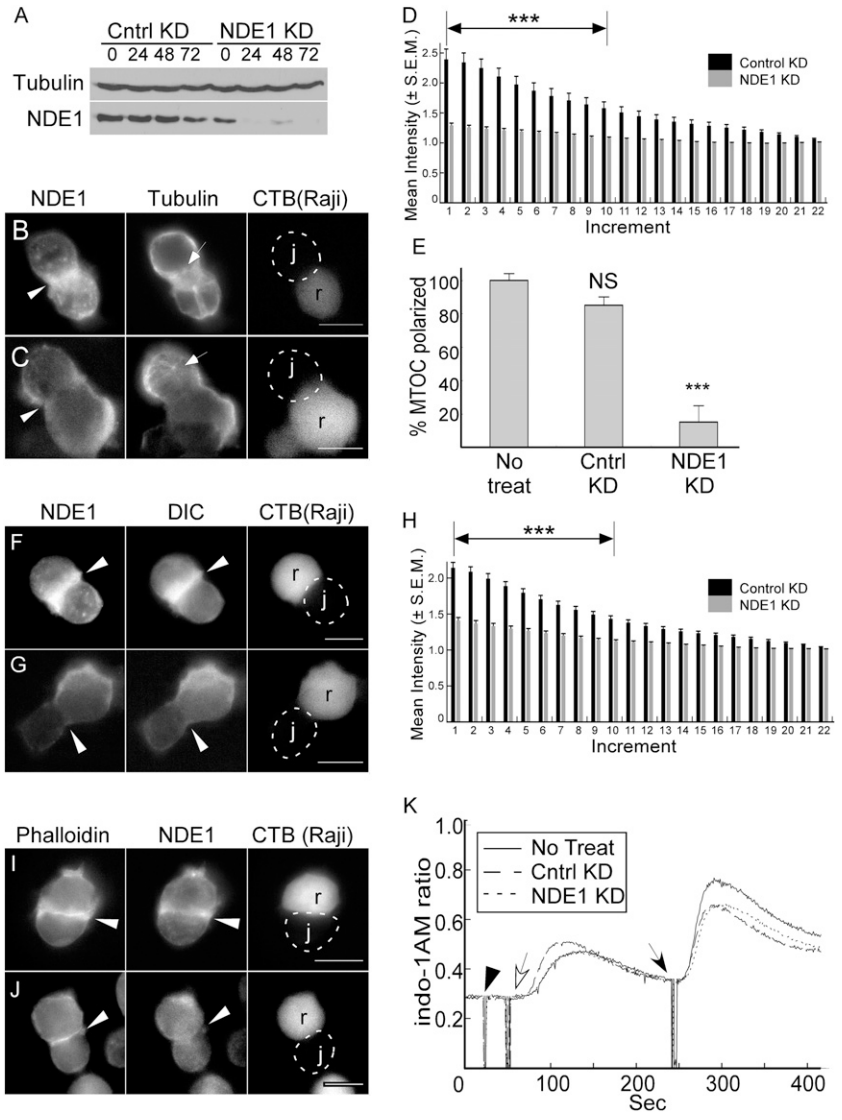

FIGURE 3. Knockdown of NDE1 in Jurkat cells. (**A**) NDE1-specific or control siRNA were electroporated into Jurkat cells and NDE1 expression was examined over 72 h after transfection on a Western blot. Jurkat/Raji pairs from either NDE1 control cells (**B**) or NDE1-specific siRNA–treated cells (**C**) were immunostained for β-tubulin and NDE1. (**D**) Mean NDE1 fluorescence ± SEM was plotted for five pixel-wide segments as described above. Data were obtained from 36 control or NDE1 siRNA–treated Jurkat/Raji cell pairs. (**E**) Immunostained Jurkat/Raji pairs were scored for MTOC polarization and plotted after background subtraction and normalization to 100%. The MTOC polarization process was significantly reduced ($p < 0.001$) in NDE1-specific siRNA–treated Jurkat cells. Jurkat/Raji paris were prepared from cells eletroporated with either control siRNA (**F**) or NDE1-specific siRNA (**G**) and immunostained for β-tubulin and the DIC. White arrowheads indicate the immunological synapse. (**H**) Mean DIC fluorescence ± SEM was plotted for five pixel-wide segments as described above. Data were derived from 36 control and NDE1 siRNA-treated Jurkat/Raji cell pairs. (**I** and **J**) Jurkat cells electroporated with either control siRNA (I) or NDE1-specific siRNA (J) paired with SEE-coated Raji cells and immunostained with anti-NDE1 Ab and for actin using TRITC-phalloidin. Raji cells were labeled with CTB; white arrowheads indicate the contact site and arrows indicate the MTOC. Scale bars, 10 μm. (**K**) Jurkat cells electroporated with control or NDE1 siRNA were loaded with indo-1-AM and stimulated with anti-Vβ8 (anti-TCR) mAb (white arrow) followed by anti-mouse Ig (dark arrow). Black arrowhead indicates stirring the cells. Data are plotted as Indo-1 emission ratios (404/485 nm), which are proportional to the free calcium ion concentration. ***$p < 0.001$.

(Fig. 5E). At a 10:1 E:T ratio, lysis was reduced from 76% for the control shRNA to 32% for CTLs receiving the N2 shRNA.

Dynactin (p150^{Glued}) is needed for secretory vesicle accumulation at the IS but not for MTOC translocation

NDE1 together with Lis1 form one of the major complexes mediating dynein-dependent transport, with the other being the dynactin complex. Using p150^{Glued} as a marker for dynactin, we monitored the distribution of dynactin both by expression of EGFP-p150^{Glued} and by immunofluorescence. In unactivated Jurkat cells, fluorescence was mainly localized to microtubules and the MTOC (data not shown). In Jurkat cells that expressed EGFP-p150^{Glued} and that were activated by SEE-coated Raji cells, EGFP-p150^{Glued} remained largely concentrated around the MTOC and along microtubules (Fig. 6A). A similar pattern of localization was seen when normal Jurkat cells were immunostained for p150^{Glued} (Fig. 6B).

We next sought to determine whether Jurkat cells had secretory lysosome-like vesicles similar to those of CTLs. Because we did not know whether Jurkat cells had similar secretory vesicles or what the contents of those vesicles might be, we expressed CTLA4 fused to mCherry as a vesicle marker. CTLA4 is a transmembrane protein resident in secretory lysosomes of CTLs (39, 40). The results show that CTLA4-labeled vesicles accumulate near the center of the synapse of activated Jurkat/Raji pairs (Supplemental Fig. 4A).

To examine the role of dynactin in MTOC translocation and vesicle movements, Jurkat cells expressing CTLA4-mCherry were electroporated with either a p150^{Glued}-specific siRNA or a scrambled control sequence and expression was monitored on Western blots. The results show that by 24 h, expression of p150^{Glued} was undetectable (Fig. 6C). Cells from the 48 h time point were then conjugated with SEE-coated Raji cells, fixed, and immunostained for tubulin and p150^{Glued}. The results show that for cells treated with the scrambled siRNA, secretory vesicles marked by CTLA4-mCherry concentrated at the IS. However, when cells were treated with p150^{Glued} siRNA, the vesicles were often dispersed around the MTOC and did not concentrate at the IS (Fig. 6D–F). The p150^{Glued}-depleted cells were also scored for MTOC translocation and the results were similar to those obtained from untreated or scrambled siRNA control cells (Fig. 6G, Supplemental Fig. 4B–D).

The finding that depletion of p150^{Glued} blocked vesicle accumulation at the IS but not MTOC translocation suggested that there is little overlap in the functions of NDE1 and dynactin in these processes. In data presented previously, immunoprecipitation of NDE1-mEGFP pulled down the DIC and Lis1 but not p150^{Glued} (Fig. 2G). The reciprocal immunoprecipitation of p150^{Glued} showed that NDE1 was not detected on the blot (Fig. 6H). Thus, our data indicate that NDE1 and p150^{Glued} are not found in the same dynein complexes. Because CTLA4 will localize to the plasma membrane

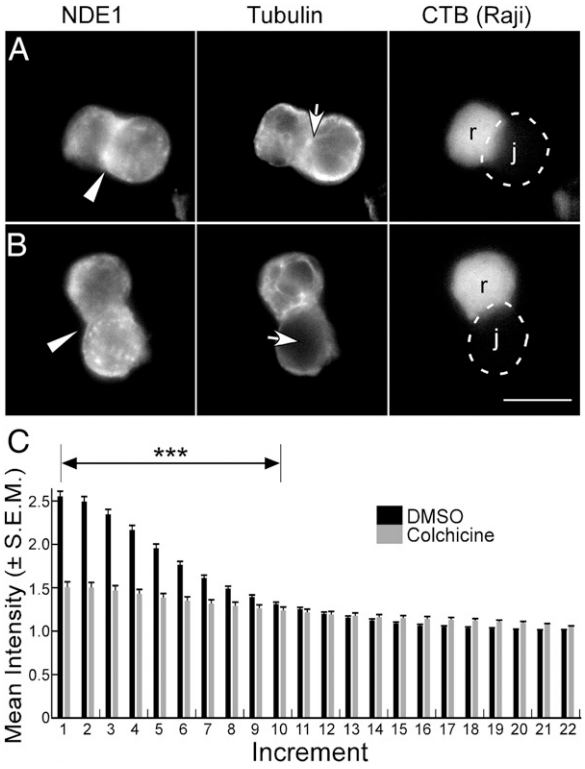

FIGURE 4. Microtubule-dependent recruitment of NDE1 to the synapse. Jurkat cells were either treated with DMSO (**A**) or 10 μM colchicine (**B**) for 15 min and then paired with SEE-coated Raji cells and immunostained for NDE1 and β-tubulin. Raji cells were labeled with CTB. White arrowheads indicate contact sites. White arrows indicate presence (top) or absence (bottom) of tubulin in Jurkat cells. Scale bar, 10 μm. (**C**) Mean NDE1 fluorescence intensity ± SEM of control and colchicine-treated cells was plotted for cell segments as described above.

upon fusion of CTLA4-containing vesicles with the membrane in activated cells, we subsequently stained for granzyme B to confirm that p150^{Glued} colocalized with secretory vesicles in mouse CTLs (Supplemental Fig. 4E).

Depletion of p150^{Glued} in mouse CTLs prevents accumulation of granzyme-containing vesicles at the synapse

We next investigated dynactin (p150^{Glued}) distribution in mouse primary CTLs. In unactivated mouse CTLs, p150^{Glued} remained largely concentrated around the MTOC and along microtubules (Supplemental Fig. 4E). Immunostaining data showed that granzyme B–containing vesicles were also clustered around the MTOC (Supplemental Fig. 4E).

We next sought to deplete p150^{Glued} in mouse CTLs. For this experiment, three shRNA target sequences were tested as was done for NDE1, and one sequence (P1) gave substantial reduction in p150^{Glued} expression (Fig. 7A). Next, we prepared CTLs that were transduced with either p150^{Glued} shRNA (P1) or a scrambled shRNA control, paired them with peptide pulsed EL4 cells, and then immunostained them for tubulin (Fig. 7B, 7C). When these p150^{Glued}-depleted conjugates were scored for MTOC translocation, the results showed no significant difference in MTOC translocation compared with those treated with the scrambled shRNA (Fig. 7D).

In control shRNA-treated cells, granzyme B–immunostained vesicles formed a distinct band or cluster at the IS whereas p150^{Glued} remained at the center of the contact site, presumably associated with the MTOC (Fig. 7E). When p150^{Glued} was depleted, accumulation of granzyme B vesicles at the IS was greatly reduced compared with those receiving a scrambled shRNA (Fig. 7F, 7G). Interestingly, in a few control knockdown cells, we observed overlapping p150^{Glued} and granzyme B signals (Supplemental Fig. 4F, 4G).

Depletion of p150^{Glued} reduces CTL-mediated cytotoxicity

Finally, we investigated how depletion of p150^{Glued} affected the ability of mouse CTLs to lyse antigenic targets. For these experiments, CTLs transduced with either p150^{Glued} or control shRNAs (as described above) were incubated for 6 h with CFSE-labeled EL4 cells in the presence or absence of peptide at various E:T ratios (1:1, 4:1, or 10:1). Subsequently, PI was added to label the dead cells. Flow cytometry was used to quantify CFSE-labeled target cells and PI-labeled dead cells as described above. Depletion of p150^{Glued} significantly inhibited CTL-mediated target cell lysis, compared with control groups (Fig. 7H). At 10:1 E:T ratios, p150^{Glued}-depleted CTLs lysis was reduced to 50% as compared with the control shRNA value of 76%.

Discussion

In this study, we examined the roles of NDE1 and dynactin in what are generally regarded as two key aspects of focused secretion: movement of the MTOC and accumulation of secretory vesicles at the IS. The results based on both expression of an inhibitory EGFP-NDE1 construct or siRNA (or shRNA)-mediated depletion of NDE1 showed that NDE1 was essential for MTOC translocation. In contrast, dynactin was not required for MTOC translocation but was needed for accumulation of secretory vesicles at the IS.

Based on immunoprecipitation of the DIC, NDE1 forms a complex with dynein and Lis1. However, the reciprocal immunoprecipitation of NDE1 pulled down Lis1 but not dynein or p150^{Glued}. This is consistent with other reports showing that immunoprecipitation of NDE1 did not pull down dynein (37). Efforts to circumvent this problem led us to construct a series of EGFP-NDE1 fusion proteins where anti-GFP Ab could be used to immunoprecipitate NDE1. This approach also avoided any confusion between NDE1 and its paralog NDEL1, which behaved quite differently insofar as NDE1 accumulated at the IS whereas NDEL1 did not (Supplemental Fig. 1F).

Four EGFP-NDE1 fusion proteins were generated and tested. Of these, both C-terminal fusion constructs accumulated at the IS as did dynein and Lis1. A slight inhibition of MTOC translocation was seen with the NDE1-EGFP but not with NDE1-mEGFP. The key difference is that in immunoprecipitation experiments, pulldown of NDE1-mEGFP brings down dynein whereas pulldowns of NDE1-EGFP did not. Immunoprecipitation of the DIC also did not pull down NDE1-EGFP even though it did pull down native NDE1. These results led to the conclusion that NDE1-EGFP does not bind to dynein.

The absence of any evidence that NDE1-EGFP binds to dynein was remarkable considering that it accumulated at the IS. Given that our data also show that NDE1 is required for accumulation of dynein at the IS, we conclude that NDE1 must be serving directly or indirectly to anchor dynein at the IS, likely through connections to the actin cytoskeleton. NDE1 normally coimmunoprecipitates with LIS1 and DISC1 and this complex could link to the actin cytoskeleton in a number of ways. DISC1 is known to interact with components of the actin cytoskeleton (26, 28, 41). Lis1 is known to form a complex with Cdc42 and CLIP-170 as well as the actin-binding protein IQGAP (42, 43). Finally, NDE1 reportedly binds to paxillin, a protein important in regulating focal adhesions and the actin cytoskeleton (44, 45).

In principle, NDE1 might accumulate at the IS by moving along microtubules, but it seems that simple diffusion and binding is not adequate in itself. Data showing that NDE1 accumulation at the IS

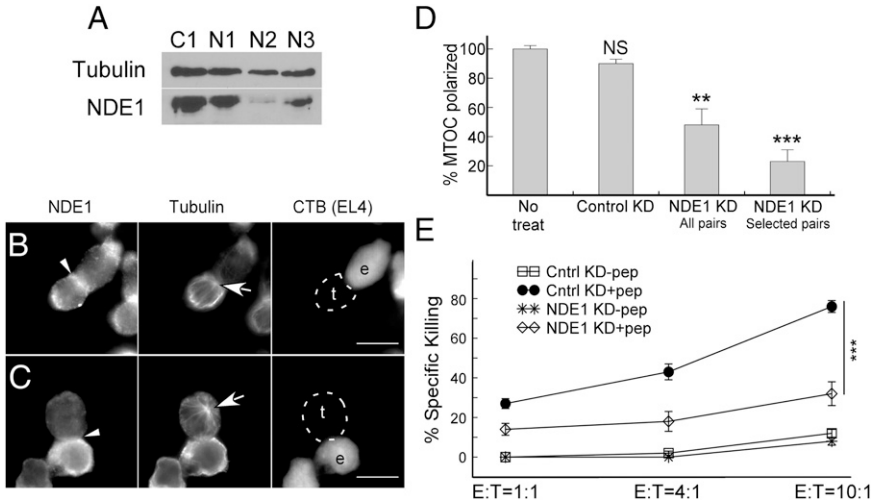

FIGURE 5. Knockdown of NDE1 in OT-I mouse CTLs. (**A**) Lentiviral particles were prepared using three different NDE1-specific shRNA sequences (N1, N2, and N3) or a scrambled shRNA control (C1) and were incubated with OT-I mouse CTL blasts. Cells were selected for puromycin resistance for 4 d, and NDE1 expression was examined on a Western blot. Cells treated with the scrambled shRNA control (**B**) and cells treated with NDE1-specific N2 shRNA (**C**) were mixed with peptide-pulsed EL4 cells, fixed, and immunostained for β-tubulin and NDE1. (**D**) Immunostained CTL-EL4 cell pairs were scored for MTOC polarization and plotted after background subtraction and normalization to 100%. For the population as a whole (unselected), MTOC polarization process was significantly reduced to ~48% ($p < 0.01$). However, MTOC polarization was seen in some cells where there was reduced but still evident NDE1 at the IS (see Supplemental Fig. 3H). When cell pairs were limited to those where no visible NDE1 was detected at the IS (selected), MTOC polarization in this subgroup was only 20% ($p < 0.001$). (**E**) NDE1 (N2)- and scrambled control (C1) shRNA–treated CTLs were mixed with EL4 target cells at different ratios for 6 h. EL4 cells were either untreated or pretreated with SIINFEKL peptide as indicated. Target cell lysis was measured by flow cytometry and is presented as specific lysis percentage of the total target cells used for each assay condition. For imaging data, EL4 cells were labeled with CTB. CTLs and EL4 cells were labeled as "t" and "e," respectively. White arrowheads indicate the contact sites; white arrows indicate the MTOC. Scale bars, 10 μm. $^{**}p < 0.01$, $^{***}p < 0.001$.

depends on intact microtubules might suggest that a motor is involved. In principle, either dynein or kinesin could carry NDE1 to the IS. However, because dynein does not seem to be required, a possible alternative is that a kinesin-like motor transports NDE1 to the IS. This seems plausible because dynein and NDE1 are known to form complexes with kinesin in other settings (7, 24, 46). Alternatively, NDE1 might be transported together with Lis1 at the tips of microtubules. Lis1 is reportedly a component of a microtubule tip-binding complex that includes CLIP-170 and IQGAP (43).

The association of NDE1 with the actin cytoskeleton would help resolve differences between dynein-dependent MTOC translocation and the model of Stinchcombe et al. (13), who proposed that an expanding actin ring at the IS drives MTOC translocation. The actin-dependent mechanism is not mutually exclusive with a role for dynein, because NDE1 and ultimately dynein likely become anchored to structures involving actin. However, we question whether actin is actually what drives MTOC translocation. For example, we showed that when a CTL is engaged with two target cells, the MTOC can oscillate between the two target contact sites (11). To generate these MTOC oscillations by the actin-based model, there would need to be coordinated cycles of microtubule release from actin anchors at one contact site and their reformation at the second site, combined with repeated cycles of actin spreading in opposite directions at the two contact sites. However, actin seems to polymerize at the center of the IS and then spreads outward to the periphery where it remains. Such a mechanism is not impossible perhaps, but is certainly harder to envision, whereas dynein-dependent oscillatory movements due to dynein are well known (47–50).

Using reciprocal immunoprecipitations and Western blots, we showed that $p150^{Glued}$ was not present with NDE1 in the same dynein complexes. This result was expected given that NDE1 and $p150^{Glued}$ bind to the same site at the N terminus of the DIC (51). This is also consistent with our data showing that NDE1 and $p150^{Glued}$ differ in their subcellular distributions. NDE1 localizes as a ring corresponding to the peripheral supramolecular activation cluster of the IS, whereas $p150^{Glued}$ is largely concentrated around the MTOC and along microtubules. However, $p150^{Glued}$ is sometimes clearly associated with granzyme B–containing vesicles. When these vesicles accumulate as a band at the IS, $p150^{Glued}$ can also be seen as a band that somewhat resembles the distribution of NDE1.

Consistent with their different distributions, NDE1 and dynactin play functionally different roles in the overall process of bringing vesicles to the IS. In an effort to study these vesicle movements, a number of methods were used to visualize acidic vesicles, but we found many more vesicles were labeled than accumulated at the IS. We decided to try labeling vesicles with CTLA4-mCherry because in CTLs, CTLA4 is known to concentrate in perforin and granzyme B–containing vesicles that move to the IS (39, 40, 52). Movement and secretion of these vesicles is ultimately what exposes CTLA4 on the surface where it can interact with B7 (53). When CTLA4-mCherry was expressed in Jurkat cells, a small subset of the total acidic vesicle pool was labeled and these vesicles accumulated at the IS when Jurkat cells engaged SEE-coated Raji cells.

In unactivated Jukat cells, many of the CTLA4-mCherry–labeled vesicles are clustered around the MTOC, and this is likely due to dynein-dependent transport (20). This is supported by our data showing that when $p150^{Glued}$ was depleted, CTLA4-labeled vesicles become more dispersed throughout the cytoplasm. However, when Jurkat cells engage SEE-coated Raji cells, even these MTOC-associated vesicles did not accumulate at the IS. Accumulation of granzyme B–containing vesicles was also reduced in $p150^{Glued}$-depleted mouse CTLs. Both sets of data indicate that $p150^{Glued}$ plays an important role in the process of focused secretion.

There are two ways $p150^{Glued}$ could play a role in bringing vesicles to the IS. One is merely to cause vesicle accumulation around the MTOC prior to MTOC translocation. In this scenario, MTOC translocation is solely responsible for bringing secretory

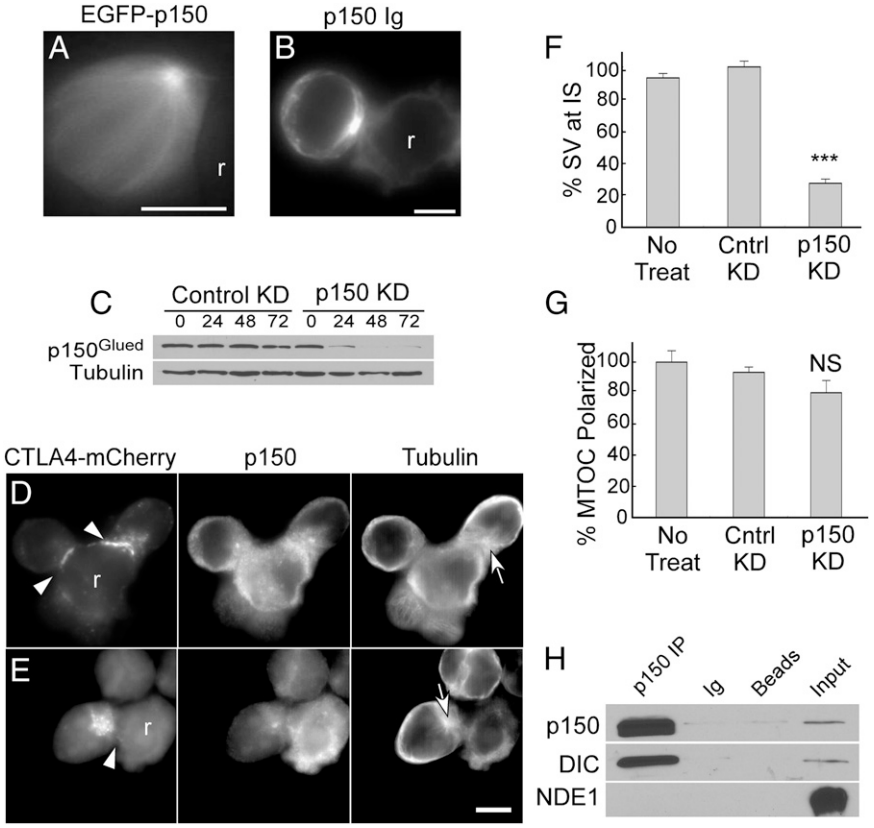

FIGURE 6. Role of p150^{Glued} in vesicle clustering and MTOC translocation. (**A** and **B**) The distribution of p150^{Glued} in Jurkat/Raji pairs was examined in live cells expressing EGFP-p150^{Glued} (A) or by immunostaining (B). (**C**) Jurkat cells expressing CTLA4-mCherry were transfected with p150^{Glued} or scrambled control siRNA and expression of p150^{Glued} at 24-h intervals after transfection was analyzed on a Western blot. CTLA4-mCherry–expressing Jurkat cells electroporated with either scrambled siRNA control (**D**) or p150^{Glued} siRNA (**E**) were paired with SEE-coated Raji cells and immunostained for β-tubulin and p150^{Glued}. (**F**) CTLA4-mCherry–expressing Jurkat cells that were electroporated with either control or p150^{Glued} siRNA were scored for vesicle clustering 48 h after transfection. The vesicle clustering was significantly reduced in Jurkat cells transfected with p150^{Glued} siRNA compared with untreated or scrambled siRNA–treated cells ($p < 0.001$). (**G**) MTOC translocation was also scored 48 h after transfection with p150^{Glued} siRNA or the scrambled control. (**H**) p150^{Glued} was immunoprecipitated from Jurkat cell lysates and blots were probed for the DIC, NDE1 and p150^{Glued}. White arrowheads indicate the contact sites; white arrows indicate MTOC. Scale bars, 5 μm. ***$p < 0.001$. r, Raji cell.

vesicles to the IS (12, 13). The other scenario is that the dynein/dynactin complex independently and perhaps continuously moves vesicles toward MTOC, and it is this movement that causes vesicle accumulation at the IS. This scenario would not eliminate the possibility that MTOC translocation brings vesicles to the IS but it also helps explain the data of Bertrand et al. (54), who showed that secretory vesicle accumulation and secretion can take place apart from MTOC translocation.

Bertrand et al. (54) noted that microtubules appear at the IS about the same time as secretory vesicles. In a previous study, we showed evidence of microtubule interaction with the IS well before the MTOC had translocated (11). Assuming that accumulation of secretory vesicles at the IS is microtubule-dependent, we propose that the initial critical step in setting up focused secretion is association of microtubules with the IS. This may be a core function of the NDE1/dynein complex. In principle, dynactin/dynein-driven vesicle movements could be in progress before, during, and after T cell activation. Were there no association of microtubules with the IS, these vesicles might simply accumulate around the MTOC. When microtubules become associated with the IS, movement of vesicles along those anchored microtubules is now directed toward the IS, a process that could begin before the MTOC translocates.

Our model does not eliminate a role for MTOC translocation in bringing vesicles to the IS but it adds flexibility such as explaining the data of Bertrand et al. (54). It also suggests a new way to think about how MTOC translocation could facilitate vesicle accumulation at the IS. In a previous study, we showed that vesicles can move along microtubules from the rear of the cell up to the IS (21). We have previously shown that microtubules form sharp turns and bend backward where they contact the IS, possibly due to dynein-driven movements (11). As the MTOC translocates, dynein-driven sliding of microtubules would cause them to move farther rearward into the cytoplasm where they might encounter new vesicles and create additional opportunities for vesicle movement toward the IS.

Yi et al. (19) reported that dynein was required for MTOC translocation, but in their studies, the process also depended on plus end microtubule depolymerization rather than sliding past the IS toward the back of the cell as we have proposed. One of the supporting evidences for their model was that taxol blocked MTOC translocation. Previous reports on the effects of taxol-related compounds are mixed, with some studies showing that they had no effect on MTOC translocation (55–57). Interestingly, note that in the study of Bertrand et al. (54), a fluorescent taxol analog was used in some experiments to label microtubules and follow MTOC translocation. Taxol does make microtubules considerably more rigid and might, at some concentrations, prevent their flexure at the IS as is required by our model (58). At present, we are not convinced that the taxol data prove that microtubule depolymerization is part of the process of MTOC translocation.

Although the model of Yi et al. (19) seems plausible, evidence is accumulating that microtubule stabilization rather than depolymerization is required for MTOC translocation. Microtubule acetylation is one of the mechanisms for increasing microtubule stability (59). Previous studies have shown that there is a burst of microtubule acetylation upon TCR ligation and that overexpression of histone deacetylase 6, which deacetylates microtubules, blocked MTOC translocation (60). Recently it has also been found that formins acetylate microtubules and that formins are required for MTOC translocation (61, 62).

We have found that both NDE1 and dynactin complexes bind to DISC1. Our preliminary data show that DISC1 localizes to mitochondria and accumulates at IS, but there is more than one isoform in Jurkat cells such that these differences might be isoform specific. Mutations in DISC1 are associated with schizophrenia and other behavioral abnormalities. It has also long been noted in the literature that immune dysfunction, and in particular T cell dysregulation, is commonly associated with schizophrenia (63, 64). Indeed, epidemiological and genetic studies have linked inflammation in general and

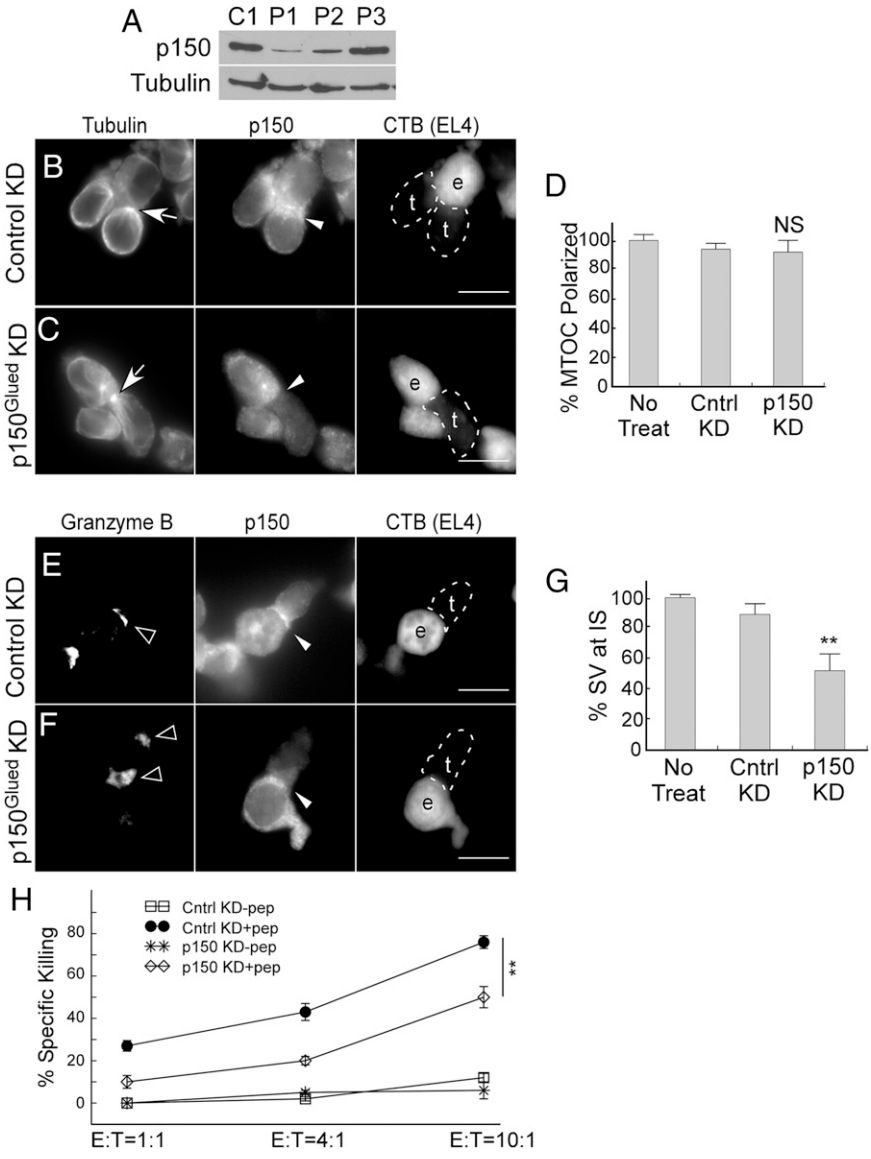

FIGURE 7. Knockdown of p150^{Glued} in OT-I transgenic mouse CTLs. (**A**) Lentiviral particles were prepared using three different p150^{Glued}-specific shRNA sequences (P1, P2, and P3) or a scrambled shRNA control (C1). Virus-transduced CTLs were selected with puromycin, and p150^{Glued} expression was analyzed on a Western blot. CTLs treated with the scrambled shRNA control (**B** and **E**) and cells treated with p150^{Glued}-specific P1 shRNA (**C** and **F**) were mixed with SIINFEKL-pulsed EL4 cells, fixed, and immunostained for β -tubulin and p150^{Glued} (B and C) or granzyme B and p150^{Glued} (E and F). Immunostained CTL-EL4 cell pairs were scored for MTOC polarization (**D**), and granzyme B–containing vesicle clustering at the IS (**G**) after background subtraction and normalization to 100% as described before. (**H**) p150^{Glued} (P1)- and scrambled control (C1) shRNA–treated CTLs were mixed with EL4 target cells at different ratios for 6 h. EL4 cells were either untreated or pretreated with SIINFEKL peptide as indicated. Target cell death was measured by flow cytometry and is presented as specific lysis percentage of the total target cells used for each assay condition. For imaging data, EL4 cells were labeled with CTB. CTLs and EL4 cells were labeled as "t" and "e," respectively. White arrowheads indicate the contact sites; white arrows indicate the MTOC; black arrowheads indicate granzyme B–containing vesicles. Scale bars, 10 μm. $^{**}p < 0.01$.

imbalanced cytokine secretion to the development of schizophrenia (65, 66). Given the association of DISC1 with neuronal secretion and the data presented in this study, perhaps DISC1 may provide a concrete link between schizophrenia and immune dysfunction.

This study shows that dynein complexed with NDE1 or p150^{Glued} performs different functions that are both important in the delivery of secretory vesicles to the IS. Furthermore, depletion of either NDE1 or p150^{Glued} had a large impact on CTL-mediated target cell lysis. Whereas NDE1 depletion had a greater impact on lysis efficiency, this might be due to the incomplete knockdown of p150^{Glued}. This study also provides hints as to how dynein might become associated with the actin cytoskeleton through the NDE1/DISC1 complex and through Lis1. Such an association could help resolve differences in various models that alternatively show that MTOC polarization depends on actin and actin-associated proteins or on dynein.

Acknowledgments

We thank Dr. Haley Tucker for critical reading of the manuscript and providing several reagents used in this study.

Disclosures

The authors have no financial conflicts of interest.

References

1. Huse, M., E. J. Quann, and M. M. Davis. 2008. Shouts, whispers and the kiss of death: directional secretion in T cells. *Nat. Immunol.* 9: 1105–1111.
2. Ueda, H., J. Zhou, J. Xie, and M. M. Davis. 2015. Distinct roles of cytoskeletal components in immunological synapse formation and directed secretion. *J. Immunol.* 195: 4117–4125.
3. Stinchcombe, J. C., M. Salio, V. Cerundolo, D. Pende, M. Arico, and G. M. Griffiths. 2011. Centriole polarisation to the immunological synapse directs secretion from cytolytic cells of both the innate and adaptive immune systems. *BMC Biol.* 9: 45.
4. Ménasché, G., J. Feldmann, A. Fischer, and G. de Saint Basile. 2005. Primary hemophagocytic syndromes point to a direct link between lymphocyte cytotoxicity and homeostasis. *Immunol. Rev.* 203: 165–179.
5. Voskoboinik, I., and J. A. Trapani. 2013. Perforinopathy: a spectrum of human immune disease caused by defective perforin delivery or function. *Front. Immunol.* 4: 441.
6. Gil-Krzewska, A., S. M. Wood, Y. Murakami, V. Nguyen, S. C. Cher Chiang, A. R. Cullinane, G. Peruzzi, W. A. Gahl, J. E. Coligan, W. J. Introne, et al. 2015. Chediak-Higashi syndrome: lysosomal trafficking regulator domains regulate exocytosis of lytic granules but not cytokine secretion by natural killer cells. *J. Allergy Clin. Immunol.* 137: 1165–1177.
7. Hackmann, Y., S. C. Graham, S. Ehl, S. Höning, K. Lehmberg, M. Aricò, D. J. Owen, and G. M. Griffiths. 2013. Syntaxin binding mechanism and disease-causing mutations in Munc18-2. *Proc. Natl. Acad. Sci. USA* 110: E4482–E4491.
8. Radoja, S., M. Saio, D. Schaer, M. Koneru, S. Vukmanovic, and A. B. Frey. 2001. CD8$^+$ tumor-infiltrating T cells are deficient in perforin-mediated cytolytic activity due to defective microtubule-organizing center mobilization and lytic granule exocytosis. *J. Immunol.* 167: 5042–5051.
9. Grakoui, A., S. K. Bromley, C. Sumen, M. M. Davis, A. S. Shaw, P. M. Allen, and M. L. Dustin. 2015. Pillars article: the immunological synapse: a molecular

machine controlling T cell activation. *Science*. 1999. 285: 221–227. *J. Immunol.* 194: 4066–4072.
10. Monks, C. R., B. A. Freiberg, H. Kupfer, N. Sciaky, and A. Kupfer. 1998. Three-dimensional segregation of supramolecular activation clusters in T cells. *Nature* 395: 82–86.
11. Kuhn, J. R., and M. Poenie. 2002. Dynamic polarization of the microtubule cytoskeleton during CTL-mediated killing. *Immunity* 16: 111–121.
12. Beal, A. M., N. Anikeeva, R. Varma, T. O. Cameron, G. Vasiliver-Shamis, P. J. Norris, M. L. Dustin, and Y. Sykulev. 2009. Kinetics of early T cell receptor signaling regulate the pathway of lytic granule delivery to the secretory domain. *Immunity* 31: 632–642.
13. Stinchcombe, J. C., E. Majorovits, G. Bossi, S. Fuller, and G. M. Griffiths. 2006. Centrosome polarization delivers secretory granules to the immunological synapse. *Nature* 443: 462–465.
14. Kupfer, A., S. L. Swain, and S. J. Singer. 1987. The specific direct interaction of helper T cells and antigen-presenting B cells. II. Reorientation of the microtubule organizing center and reorganization of the membrane-associated cytoskeleton inside the bound helper T cells. *J. Exp. Med.* 165: 1565–1580.
15. Poo, W. J., L. Conrad, and C. A. Janeway, Jr. 1988. Receptor-directed focusing of lymphokine release by helper T cells. *Nature* 332: 378–380.
16. Cianfrocco, M. A., M. E. DeSantis, A. E. Leschziner, and S. L. Reck-Peterson. 2015. Mechanism and regulation of cytoplasmic dynein. *Annu. Rev. Cell Dev. Biol.* 31: 83–108.
17. Combs, J., S. J. Kim, S. Tan, L. A. Ligon, E. L. Holzbaur, J. Kuhn, and M. Poenie. 2006. Recruitment of dynein to the Jurkat immunological synapse. *Proc. Natl. Acad. Sci. USA* 103: 14883–14888.
18. Martín-Cófreces, N. B., J. Robles-Valero, J. R. Cabrero, M. Mittelbrunn, M. Gordón-Alonso, C. H. Sung, B. Alarcón, J. Vázquez, and F. Sánchez-Madrid. 2008. MTOC translocation modulates IS formation and controls sustained T cell signaling. *J. Cell Biol.* 182: 951–962.
19. Yi, J., X. Wu, A. H. Chung, J. K. Chen, T. M. Kapoor, and J. A. Hammer. 2013. Centrosome repositioning in T cells is biphasic and driven by microtubule end-on capture-shrinkage. *J. Cell Biol.* 202: 779–792.
20. Mentlik, A. N., K. B. Sanborn, E. L. Holzbaur, and J. S. Orange. 2010. Rapid lytic granule convergence to the MTOC in natural killer cells is dependent on dynein but not cytolytic commitment. *Mol. Biol. Cell* 21: 2241–2256.
21. Poenie, M., J. Kuhn, and J. Combs. 2004. Real-time visualization of the cytoskeleton and effector functions in T cells. *Curr. Opin. Immunol.* 16: 428–438.
22. Soares, D. C., N. J. Bradshaw, J. Zou, C. K. Kennaway, R. S. Hamilton, Z. A. Chen, M. A. Wear, E. A. Blackburn, J. Bramham, B. Böttcher, et al. 2012. The mitosis and neurodevelopment proteins NDE1 and NDEL1 form dimers, tetramers, and polymers with a folded back structure in solution. *J. Biol. Chem.* 287: 32381–32393.
23. Schroer, T. A. 2004. Dynactin. *Annu. Rev. Cell Dev. Biol.* 20: 759–779.
24. Taya, S., T. Shinoda, D. Tsuboi, J. Asaki, K. Nagai, T. Hikita, S. Kuroda, K. Kuroda, M. Shimizu, S. Hirotsune, et al. 2007. DISC1 regulates the transport of the NUDEL/LIS1/14-3-3ε complex through kinesin-1. *J. Neurosci.* 27: 15–26.
25. Okamoto, M., T. Iguchi, T. Hattori, S. Matsuzaki, Y. Koyama, M. Taniguchi, M. Komada, M. J. Xie, H. Yagi, S. Shimizu, et al. 2015. DBZ regulates cortical cell positioning and neurite development by sustaining the anterograde transport of Lis1 and DISC1 through control of Ndel1 dual-phosphorylation. *J. Neurosci.* 35: 2942–2958.
26. Steinecke, A., C. Gampe, F. Nitzsche, and J. Bolz. 2014. DISC1 knockdown impairs the tangential migration of cortical interneurons by affecting the actin cytoskeleton. *Front. Cell. Neurosci.* 8: 190.
27. Thomson, P. A., E. L. Malavasi, E. Grünewald, D. C. Soares, M. Borkowska, and J. K. Millar. 2013. DISC1 genetics, biology and psychiatric illness. *Front. Biol. (Beijing)* 8: 1–31.
28. Wang, Q., and N. J. Brandon. 2011. Regulation of the cytoskeleton by disrupted-in-schizophrenia 1 (DISC1). *Mol. Cell. Neurosci.* 48: 359–364.
29. Flores III, R., Y. Hirota, B. Armstrong, A. Sawa, and T. Tomoda. 2011. DISC1 regulates synaptic vesicle transport via a lithium-sensitive pathway. *Neurosci. Res.* 71: 71–77.
30. Bradshaw, N. J., and D. J. Porteous. 2012. DISC1-binding proteins in neural development, signalling and schizophrenia. *Neuropharmacology* 62: 1230–1241.
31. Hattori, T., S. Shimizu, Y. Koyama, K. Yamada, R. Kuwahara, N. Kumamoto, S. Matsuzaki, A. Ito, T. Katayama, and M. Tohyama. 2010. DISC1 regulates cell-cell adhesion, cell-matrix adhesion and neurite outgrowth. *Mol. Psychiatry* 15: 778–798–809.
32. Moffat, J., D. A. Grueneberg, X. Yang, S. Y. Kim, A. M. Kloepfer, G. Hinkle, B. Piqani, T. M. Eisenhaure, B. Luo, J. K. Grenier, et al. 2006. A lentiviral RNAi library for human and mouse genes applied to an arrayed viral high-content screen. *Cell* 124: 1283–1298.
33. Mattis, A. E., G. Bernhardt, M. Lipp, and R. Förster. 1997. Analyzing cytotoxic T lymphocyte activity: a simple and reliable flow cytometry-based assay. *J. Immunol. Methods* 204: 135–142.
34. Purbhoo, M. A., D. J. Irvine, J. B. Huppa, and M. M. Davis. 2004. T cell killing does not require the formation of a stable mature immunological synapse. *Nat. Immunol.* 5: 524–530.
35. Stowers, L., D. Yelon, L. J. Berg, and J. Chant. 1995. Regulation of the polarization of T cells toward antigen-presenting cells by Ras-related GTPase CDC42. *Proc. Natl. Acad. Sci. USA* 92: 5027–5031.
36. Quann, E. J., E. Merino, T. Furuta, and M. Huse. 2009. Localized diacylglycerol drives the polarization of the microtubule-organizing center in T cells. *Nat. Immunol.* 10: 627–635.
37. Stehman, S. A., Y. Chen, R. J. McKenney, and R. B. Vallee. 2007. NudE and NudEL are required for mitotic progression and are involved in dynein recruitment to kinetochores. *J. Cell Biol.* 178: 583–594.
38. Campbell, R. E., O. Tour, A. E. Palmer, P. A. Steinbach, G. S. Baird, D. A. Zacharias, and R. Y. Tsien. 2002. A monomeric red fluorescent protein. *Proc. Natl. Acad. Sci. USA* 99: 7877–7882.
39. Linsley, P. S., J. Bradshaw, J. Greene, R. Peach, K. L. Bennett, and R. S. Mittler. 1996. Intracellular trafficking of CTLA-4 and focal localization towards sites of TCR engagement. *Immunity* 4: 535–543.
40. Iida, T., H. Ohno, C. Nakaseko, M. Sakuma, M. Takeda-Ezaki, H. Arase, E. Kominami, T. Fujisawa, and T. Saito. 2000. Regulation of cell surface expression of CTLA-4 by secretion of CTLA-4-containing lysosomes upon activation of $CD4^+$ T cells. *J. Immunol.* 165: 5062–5068.
41. Goudarzi, S., L. J. Smith, S. Schütz, and S. Hafizi. 2013. Interaction of DISC1 with the PTB domain of Tensin2. *Cell. Mol. Life Sci.* 70: 1663–1672.
42. Kholmanskikh, S. S., H. B. Koeller, A. Wynshaw-Boris, T. Gomez, P. C. Letourneau, and M. E. Ross. 2006. Calcium-dependent interaction of Lis1 with IQGAP1 and Cdc42 promotes neuronal motility. *Nat. Neurosci.* 9: 50–57.
43. Coquelle, F. M., M. Caspi, F. P. Cordelières, J. P. Dompierre, D. L. Dujardin, C. Koifman, P. Martin, C. C. Hoogenraad, A. Akhmanova, N. Galjart, et al. 2002. LIS1, CLIP-170's key to the dynein/dynactin pathway. *Mol. Cell. Biol.* 22: 3089–3102.
44. Shan, Y., L. Yu, Y. Li, Y. Pan, Q. Zhang, F. Wang, J. Chen, and X. Zhu. 2009. Nudel and FAK as antagonizing strength modulators of nascent adhesions through paxillin. *PLoS Biol.* 7: e1000116.
45. Deakin, N. O., and C. E. Turner. 2008. Paxillin comes of age. *J. Cell Sci.* 121: 2435–2444.
46. Roberts, A. J., B. S. Goodman, and S. L. Reck-Peterson. 2014. Reconstitution of dynein transport to the microtubule plus end by kinesin. *ELife* 3: e02641.
47. Yeh, E., R. V. Skibbens, J. W. Cheng, E. D. Salmon, and K. Bloom. 1995. Spindle dynamics and cell cycle regulation of dynein in the budding yeast, *Saccharomyces cerevisiae. J. Cell Biol.* 130: 687–700.
48. Yamamoto, A., R. R. West, J. R. McIntosh, and Y. Hiraoka. 1999. A cytoplasmic dynein heavy chain is required for oscillatory nuclear movement of meiotic prophase and efficient meiotic recombination in fission yeast. *J. Cell Biol.* 145: 1233–1249.
49. Vogel, S. K., N. Pavin, N. Maghelli, F. Jülicher, and I. M. Tolić-Nørrelykke. 2009. Self-organization of dynein motors generates meiotic nuclear oscillations. *PLoS Biol.* 7: e1000087.
50. Yamamoto, A., C. Tsutsumi, H. Kojima, K. Oiwa, and Y. Hiraoka. 2001. Dynamic behavior of microtubules during dynein-dependent nuclear migrations of meiotic prophase in fission yeast. *Mol. Biol. Cell* 12: 3933–3946.
51. McKenney, R. J., S. J. Weil, J. Scherer, and R. B. Vallee. 2011. Mutually exclusive cytoplasmic dynein regulation by NudE-Lis1 and dynactin. *J. Biol. Chem.* 286: 39615–39622.
52. Miranda, L. R., B. C. Schaefer, A. Kupfer, Z. Hu, and A. Franzusoff. 2002. Cell surface expression of the HIV-1 envelope glycoproteins is directed from intracellular CTLA-4-containing regulated secretory granules. *Proc. Natl. Acad. Sci. USA* 99: 8031–8036.
53. Chen, L., S. Ashe, W. A. Brady, I. Hellström, K. E. Hellström, J. A. Ledbetter, P. McGowan, and P. S. Linsley. 1992. Costimulation of antitumor immunity by the B7 counterreceptor for the T lymphocyte molecules CD28 and CTLA-4. *Cell* 71: 1093–1102.
54. Bertrand, F., S. Müller, K. H. Roh, C. Laurent, L. Dupré, and S. Valitutti. 2013. An initial and rapid step of lytic granule secretion precedes microtubule organizing center polarization at the cytotoxic T lymphocyte/target cell synapse. *Proc. Natl. Acad. Sci. USA* 110: 6073–6078.
55. Knox, J. D., R. E. Mitchel, and D. L. Brown. 1993. Effects of taxol and taxol/hyperthermia treatments on the functional polarization of cytotoxic T lymphocytes. *Cell Motil. Cytoskeleton* 24: 129–138.
56. Mehta, S., D. Blackinton, M. Manfredi, D. Rajaratnam, N. Kouttab, and H. Wanebo. 1997. Taxol pretreatment of tumor targets amplifies natural killer cell mediated lysis. *Leuk. Lymphoma* 26: 67–76.
57. Chuang, L. T., E. Lotzová, J. Heath, K. R. Cook, A. Munkarah, M. Morris, and J. T. Wharton. 1994. Alteration of lymphocyte microtubule assembly, cytotoxicity, and activation by the anticancer drug taxol. *Cancer Res.* 54: 1286–1291.
58. Mickey, B., and J. Howard. 1995. Rigidity of microtubules is increased by stabilizing agents. *J. Cell Biol.* 130: 909–917.
59. Kull, F. J., and R. D. Sloboda. 2014. A slow dance for microtubule acetylation. *Cell* 157: 1255–1256.
60. Valenzuela-Fernández, A., J. R. Cabrero, J. M. Serrador, and F. Sánchez-Madrid. 2008. HDAC6: a key regulator of cytoskeleton, cell migration and cell–cell interactions. *Trends Cell Biol.* 18: 291–297.
61. Gomez, T. S., K. Kumar, R. B. Medeiros, Y. Shimizu, P. J. Leibson, and D. D. Billadeau. 2007. Formins regulate the actin-related protein 2/3 complex-independent polarization of the centrosome to the immunological synapse. *Immunity* 26: 177–190.
62. Thurston, S. F., W. A. Kulacz, S. Shaikh, J. M. Lee, and J. W. Copeland. 2012. The ability to induce microtubule acetylation is a general feature of formin proteins. *PLoS One* 7: e48041.
63. Debnath, M. 2015. Adaptive immunity in schizophrenia: functional implications of T cells in the etiology, course and treatment. *J. Neuroimmune Pharmacol.* 10: 610–619.
64. Khandaker, G. M., L. Cousins, J. Deakin, B. R. Lennox, R. Yolken, and P. B. Jones. 2015. Inflammation and immunity in schizophrenia: implications for pathophysiology and treatment. *Lancet Psychiatry* 2: 258–270.
65. Khandaker, G. M., and R. Dantzer. 2015. Is there a role for immune-to-brain communication in schizophrenia? *Psychopharmacology (Berl)* 233: 1559–1573.
66. Altamura, A. C., S. Pozzoli, A. Fiorentini, and B. Dell'osso. 2013. Neurodevelopment and inflammatory patterns in schizophrenia in relation to pathophysiology. *Prog. Neuropsychopharmacol. Biol. Psychiatry* 42: 63–70.

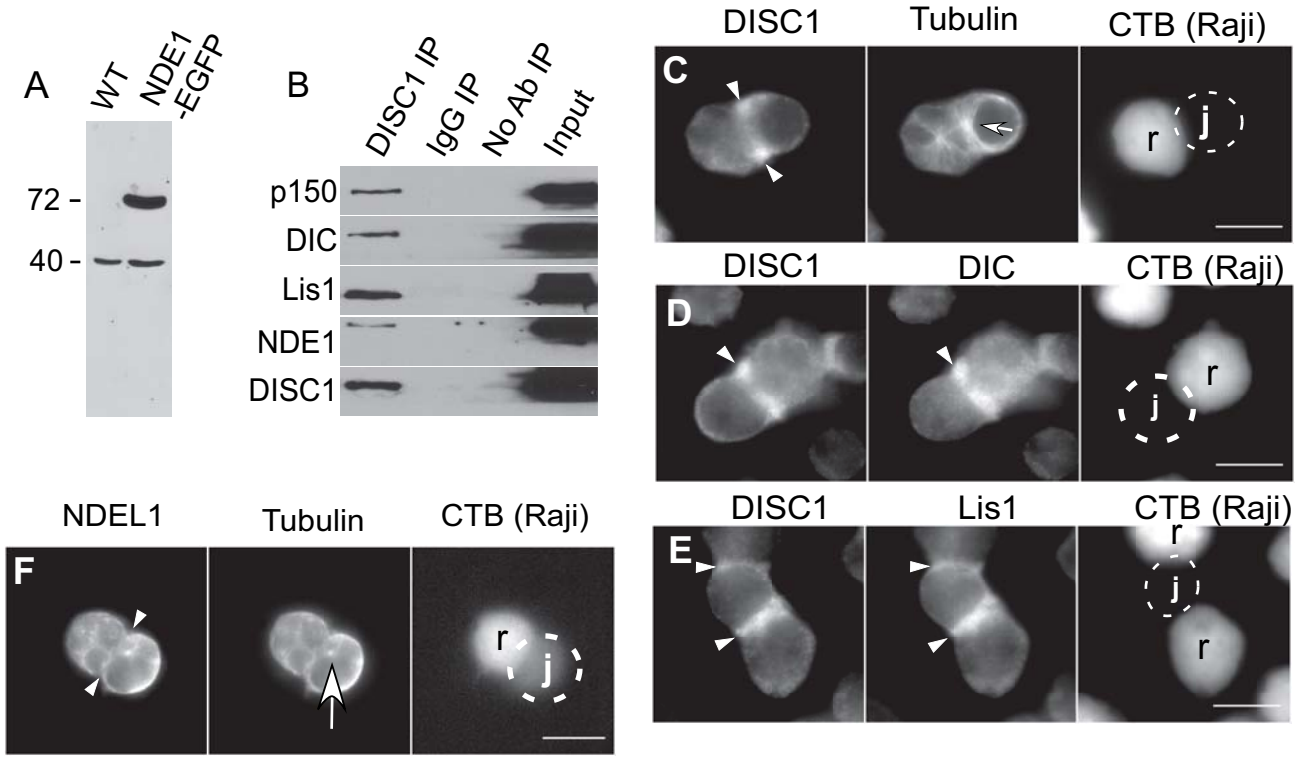

Supplemental Figure 1. NDE1, DISC1 and NDEL1 in Jurkat cells

(A) Western blots from normal Jurkat cell lysates or those expressing NDE1-EGFP were probed for NDE1. (B) DISC1 immunoprecipitates from Jurkat cell lysates were probed for Lis1, the DIC, NDE1 and $p150^{Glued}$. 15% of the supernatant of the immunoprecipitation reaction was loaded in the 'input' lane. (C-E) The localization of DISC1, Lis1 and dynein were compared by immunostaining Jurkat-Raji pairs for (C) DISC1 and β-tubulin, (D) DISC1 and the DIC, (E) DISC1 and Lis1. (F) Jurkat cells were activated by pairing with SEE-coated Raji B cells, fixed, and immunostained using rat anti-NDEL1 antibody and β-tubulin. White arrow head indicates the contact site while white arrows indicate polarized MTOC. Raji cells were stained with CTB. 'r' stands Raji cell, 'j' stands for Jurkat cell. Scale bar is 10 μm.

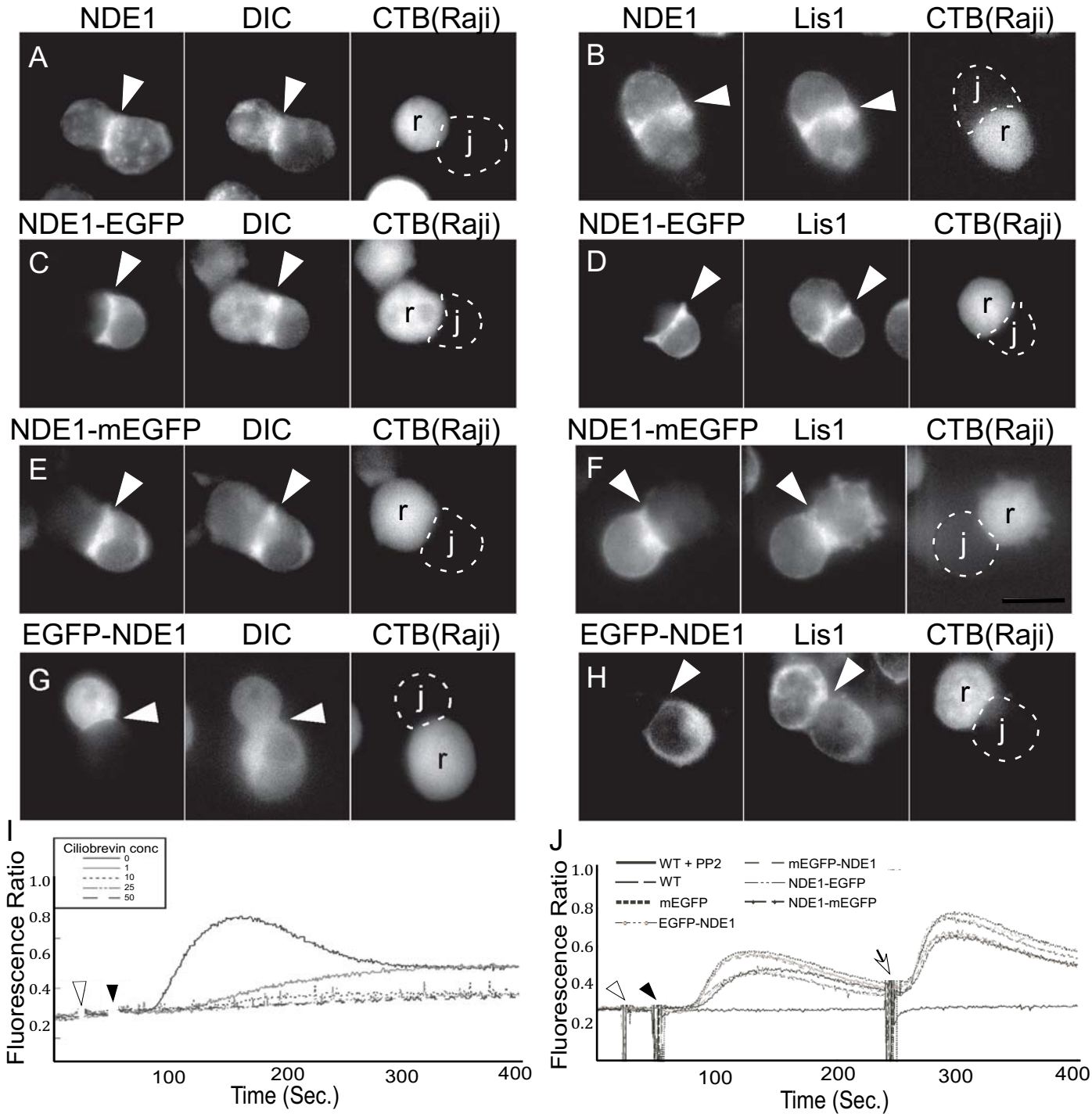

Supplemental figure 2. NDE1, Lis1 and DIC at the junction (IS) of Jurkat-Raji pairs.
NDE1 and the DIC (A) or Lis1 (B) were localized by immunofluorescence. Fluorescence of expressed NDE1 GFP constructs was compared to immunostains for the DIC or Lis1, (C) NDE1-EGFP: the DIC; (D) NDE1-EFGP:Lis1; (E) NDE1-mEGFP:DIC; (F) NDE1-mEGFP:Lis1; (G) EGFP-NDE1:DIC; (H) EGFP-NDE1: Lis1. Raji cells were labeled with CTB. 'r' stands Raji cell, 'j'stands for Jurkat cell. White arrow heads indicate the contact site. Scale bar is 10 μm. (I,J) Jurkat cells were loaded with indo-1-AM after incubation with different concentrations of Ciliobrevin and stimulated anti-TCR Ig (dark arrow head). (J) Jurkat cells expressing various NDE1-fusion proteins were loaded with indo-1-AM and stimulated by anti-TCR antibody (dark arrow head) and subsequently by a secondary cross linking antibody (white arrow).

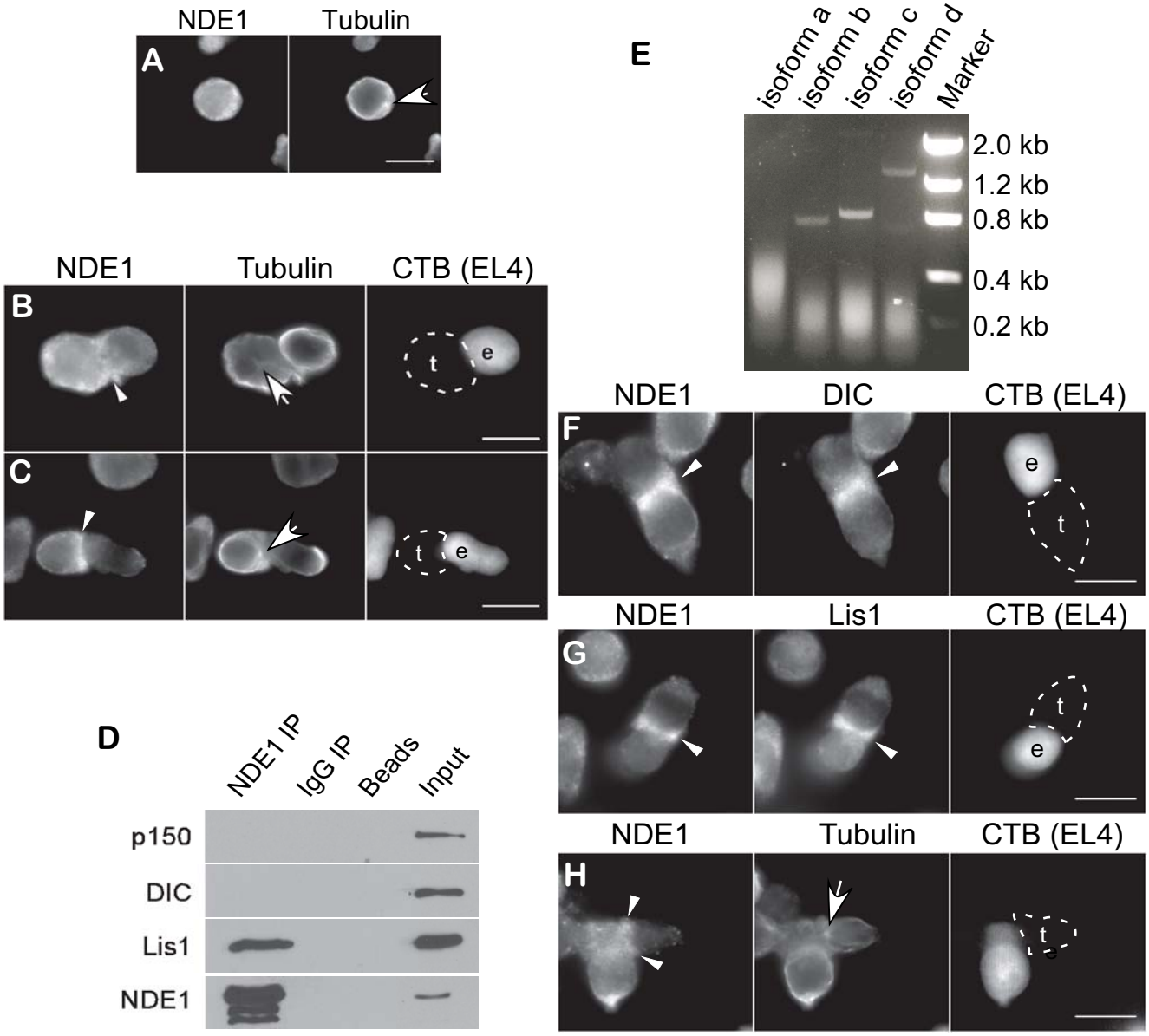

Supplemental figure 3. NDE1 in OT-I CTLs

(A) OT-I primary mouse CTLs were fixed and immunostained for NDE1 and β-tubulin. (B) CTLs were paired with either untreated EL4 cells or (C) SIINFEKL-pulsed EL4 cells, and immunostained for NDE1 and β-tubulin. (D) NDE1 was immunoprecipitated from CTL lysates using anti-NDE1 antibody and then blots were probed for Lis1, the DIC and $p150^{Glued}$. (E) Polymerase chain reactions were performed to test presence of NDE1 isoform a, b, c and d in OT-I primary CTL cDNA library. The colocalization of NDE1, Lis1 and dynein (DIC) were compared by immunostaining CTL-SIINFEKL-pulsed EL4 cell pairs for (F) NDE1 and DIC or (G) NDE1 and Lis1. (H) NDE1 expression was depleted in CTL and then activated by peptide pulsed EL4 cells. EL4 cells were stained with CTB. 'e' stands EL4 cell, 't' stands for cytotoxic T lymphocyte. Scale bar is 10 μm.

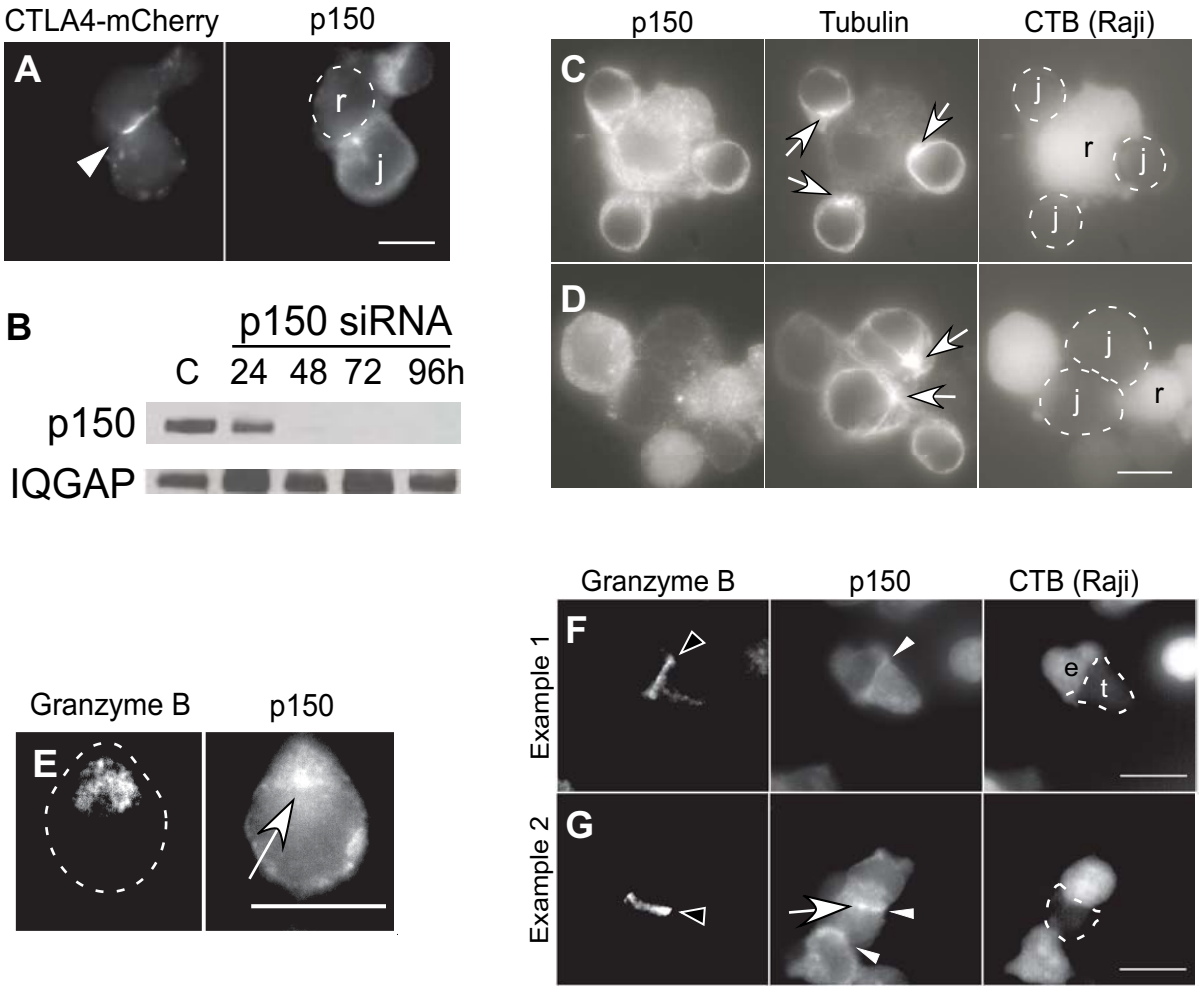

Supplemental figure 4. Knockdown of p150^{Glued}

(A) CTLA4-mCherry expressing Jurkat cells were paired with SEE-coated Raji cells and immunostained for p150^{Glued}. White arrow head indicates contact site. (B) Jurkat T cells were electroporated with p150^{Glued} siRNA or a scrambled control siRNA. Expression of p150^{Glued} was determined by Western blots. (C-D) 48 hours after electroporation, Jurkats were conjugated with SEE-labeled Raji cells stained with CTB, fixed, and immunostained with β-tubulin and p150^{Glued} antibodies. Tubulin staining showed that MTOC polarization was normal in p150^{Glued} knock-down cells (D) when compared to controls (C). OT-I mouse CTLs were either untreated (E) or activated by peptide pulsed EL4 cells (F-G) and immunostained for granzyme B and p150^{Glued}. White arrow heads indicate the contact sites, white arrows indicate MTOC, black arrow heads indicate granzyme B-containing vesicles. EL4 cells were stained with CTB. 'e' stands EL4 cell, 't' stands for cytotoxic T lymphocyte. Scale bar is 10 μm.